

# Functional additive regression on shape and form manifolds of planar curves

Almond Stöcker      Sonja Greven

Humboldt Universität zu Berlin

## Abstract

Defining shape and form as equivalence classes under translation, rotation and – for shapes – also scale, we extend generalized additive regression to models for the shape/form of planar curves or landmark configurations. The model respects the resulting quotient geometry of the response, employing the squared geodesic distance as loss function and a geodesic response function mapping the additive predictor to the shape/form space. For fitting the model, we propose a Riemannian  $L_2$ -Boosting algorithm well-suited for a potentially large number of possibly parameter-intensive model terms, which also yields automated model selection. We provide novel intuitively interpretable visualizations for (even non-linear) covariate effects in the shape/form space via suitable tensor-product factorization. The usefulness of the proposed framework is illustrated in an analysis of 1) astragalus shapes of wild and domesticated sheep and 2) cell forms generated in a biophysical model, as well as 3) in a realistic simulation study with response shapes and forms motivated from a dataset on bottle outlines.

**functional data, shape data, additive regression, Boosting, visualization**

## 1 Introduction

In many imaging data problems, the coordinate system of recorded objects is arbitrary or explicitly not of interest. Statistical shape analysis (Dryden and Mardia, 2016) addresses this point by identifying the ultimate object of analysis as the ‘shape’ of an observation, reflecting its geometric properties invariant under translation, rotation and re-scaling, or as its ‘form’ (or ‘size-and-shape’) invariant only under translation and rotation. This paper establishes an interpretable and flexible additive regression framework for modeling the shape or form of planar curves and/or landmark configurations in dependence on scalar covariates. The framework directly extends additive models for scalar response, providing for instance smooth effects of multiple covariates, while intrinsically accounting for the geometry of the quotient space. With the proposed component-wise Riemannian  $L_2$ -Boosting algorithm, a potentially large number of parameter-intensive model terms can be estimated with inherent model selection. We further propose a tensor-product factorization based on singular value decomposition (SVD) for visualizing estimated effects, which we consider essential for practical interpretation. We concentrate on the functional case of curves, but analysis of landmark shapes or forms is contained as a special case. In particular, the regression framework is suitable for relatively sparsely and irregularly sampled response curves.

A rich literature on ‘classical’ statistical shape analysis has been developed for 2D or 3D landmark configurations, presenting for instance selected points of a bone or face, which are considered elements of Kendall’s shape space (see, e.g. Dryden and Mardia, 2016). Methods include

Generalized Procrustes algorithms (e.g., Goodall, 1991) for alignment and mean computation, as well as Principal Component Analysis (Kent, 1994), and inference procedures based on shape distributions (e.g., Kent, 1994; Mardia and Dryden, 1989). In contrast to standard multivariate statistics, these usually involve differential geometric tools due to the non-linearity of the arising landmark shape space (Kendall, 1984). In many 2D scenarios, however, observed points describe a curve reflecting the outline of an object rather than dedicated landmarks. Approaches for outline analysis in the morphometrics literature include basis representations, with, e.g., Fourier or discrete cosine transformations, transferring the analysis of the shapes themselves to the analysis of vectors of basis coefficients (e.g. Rohlf and Archie, 1984; Dommergues et al., 2007), and semi-landmark analysis (compare Adams et al., 2013) where points on the outline curves are allowed to slide tangentially along the curves to increase their comparability. More generally, considering outlines as images of (parameterized) curves shows a direct connection to functional data analysis (FDA, Ramsay and Silverman, 2005). Considering observed curves elements of a Hilbert space of multi-dimensional functions, it is a common approach in FDA to utilize a suitable (smooth) function basis for modelling. Unlike classical landmark shape analysis, we will take the more general FDA perspective and speak of functional shape/form data (analysis) in this context. From the FDA perspective, the problem of matching comparable points along an outline translates to a registration problem of finding appropriate curve parameterizations attributing the same index to corresponding points. The square root velocity framework (Srivastava and Klassen, 2016) has attracted considerable attention in this context offering ‘elastic’ analysis of functional shapes modulo re-parameterization (“warping”). Although we do not consider elastic methodology here assuming suitable parameterizations fixed and known, strong methodical intersections suggest viewing present investigations as an important step towards corresponding elastic regression. With respect to the sampling design, FDA literature distinguishes *regular* designs, where functional data is evaluated on a common grid, from *irregular* functional data designs corresponding to curve data where parameterized curves are evaluated on different grids, i.e. points recorded along two outlines do not fully correspond. While in the regular case, analysis often simplifies by treating curve evaluations as multivariate data, more general irregular designs gave rise to further developments in FDA (e.g. Yao et al., 2005; Greven and Scheipl, 2017) explicitly considering irregular measurements instead of interpolating original observations to fit a regular design. However, tight to a functional perspective, approaches for irregular designs did, as far as we know, not enter shape analysis literature previous to our paper.

Starting from geodesic regression (Fletcher, 2013; Fishbaugh et al., 2013), which extends linear regression to curved spaces, several authors have developed generalizations of standard regression models to manifold data responses, such as MANOVA (Huckemann et al., 2010), polynomial regression (Hinkle et al., 2014), regression along geodesic paths with non-constant speed (Hong et al., 2014), or kernel regression (Davis et al., 2010). While these methods are formulated more generally, landmark shape spaces often serve as an example for application. However, they consider only one metric or categorical covariate. By contrast, Zhu et al. (2009); Shi et al. (2009); Kim et al. (2014) generalize geodesic regression to regression with multiple covariates but with symmetric positive-definite (SPD) matrices as response rather than shapes. Cornea et al. (2017) further conceptualize these approaches to a generalized linear model (GLM) analogue regression framework for responses in a symmetric space – a class of Riemannian manifolds containing, in particular, Kendall’s shape space – and apply it for shape analysis. Recently, Lin et al. (2020) proposed a Lie group additive regression model for Riemannian manifolds focusing however on SPD matrices and not on shapes.

In FDA, there is a much wider range of developed regression methods (see overviews in Morris, 2015; Greven and Scheipl, 2017) addressing, in particular, also irregular curve-specific and potentially sparse measurement grids (e.g. Yao et al., 2005; Cederbaum et al., 2016). Among

the most flexible models for (univariate) functional responses are the functional additive mixed models (FAMMs) of i.a. Morris and Carroll (2006); Meyer et al. (2015) for dense functional data and the flexible FAMM model class also covering sparse functional data, summarized in Greven and Scheipl (2017). There is less work on regression for bivariate or multivariate functional responses. Rosen and Thompson (2009); Zhu et al. (2012); Olsen et al. (2018) consider linear fixed effects of scalar covariates, the latter also allowing for warping. Goldsmith and Kitago (2016); Zhu et al. (2017); Backenroth et al. (2018) consider one or more random effects for one grouping variable, linear fixed effects and common dense grids for all functions. Volkmann et al. (2021) combine the FAMM model class of Greven and Scheipl (2017) with multivariate functional principal component analysis (MFPCA, Chiou et al. (2014), Happ and Greven (2018)) for regression with multivariate functional responses.

Brockhaus et al. (2015) employ a (component-wise) model-based gradient boosting algorithm for estimating FAMMs. Model-based boosting (Bühlmann and Hothorn, 2007) is a stage-wise fitting procedure for estimating additive regression models with inherent model selection and a slow over-fitting behavior, allowing to efficiently estimate models with a very large number of coefficients. Regularization is applied both in each step and via early stopping of the algorithm based, e.g., on cross-validation. The combination of high auto-correlation within functional responses and complex tensor-product covariate effects typical for FAMMs make the double regularization particularly beneficial in this context (Stöcker et al., 2021). Gradient boosting with respect to a least-squares loss is typically referred to as  $L^2$ -Boosting (Bühlmann and Yu, 2003).

We introduce a Riemannian  $L^2$ -Boosting algorithm for estimating additive regression models for response shapes/forms of planar curves living in quotient spaces with respect to translation, rotation and potentially re-scaling. We thereby extend GLM-type intrinsic regression for manifold-valued responses (Cornea et al., 2017) to additive models allowing for smooth covariate effects and for functional shape responses, while offering suitable means of regularization to face high-dimensional modeling. In particular, the approach includes analysis of irregular functional shape data evaluated on varying grids. Although frequently occurring in real-life outline data, we are not aware of any other explicit treatment of this case in literature to date. We propose an SVD-based visualization technique, factorizing estimated tensor-product effects into intuitively interpretable directions of shape/form change on the one hand and conventional additive effects into that direction on the other hand.

Thus, the four major contributions of our regression framework are: 1. generalization of classical approaches of shape and functional data analysis to intrinsic regression for (irregularly sampled) functional shape and form responses, allowing to specify smooth covariate effects in an additive model predictor, 2. a novel Riemannian  $L_2$ -Boosting algorithm for estimating additive regression models for this type of manifold response, and 3. a visualization technique yielding intuitive interpretations even of multi-dimensional smooth covariate effects for practitioners. This visualization has not been used before, although we see potential usefulness also for other functional regression models. Despite our focus on shapes and forms, transfer of the model, Riemannian  $L_2$ -Boosting, and factorized visualization to other Riemannian manifold responses is intended in the generality of the formulation and the design of the provided R package `manifoldboost` (developer version on [github.com/Almond-S/manifoldboost](https://github.com/Almond-S/manifoldboost)). The versatile applicability of the approach is illustrated in three different scenarios: an analysis of the shape of sheep astragali (ankle bones) represented by both regularly sampled curves and landmarks in dependence on categorical 'demographic' variables; an analysis of the effects of different metric biophysical model parameters on the form of (irregularly sampled) cell outlines generated from a cellular Potts model, including also smooth covariate interaction terms; and a simulation study with irregularly sampled functional shape and form responses generated from a dataset of different

bottle outlines and including metric and categorical covariates.

The remainder of the paper is structured as follows: in Section 2, we introduce the manifold geometry of irregular curves modulo translation, rotation and potentially re-scaling, necessary to define the response space of the intrinsic additive regression model formulated in Section 3. The model-based Riemannian  $L^2$ -Boosting algorithm is introduced in Section 4. We apply the regression framework to analyze different data problems in Section 5 modeling sheep bone shape responses (Section 5.1) and cell outlines (Section 5.2). Section 5.3 summarizes the results of a simulation study with functional shape and form responses. We conclude the paper with a discussion in Section 6.

## 2 Geometry of functional forms and shapes

In this section, we introduce the necessary geometric background for functional regression with shapes and forms as responses. Riemannian manifolds of planar shapes (and forms) are discussed in various textbooks at different levels of generality, in finite (Dryden and Mardia, 2016; Kendall et al., 1999) or potentially in-finite dimensions (Srivastava and Klassen, 2016; Klingenberg, 1995). The shape and the form of a planar curve  $y : [0, 1] \rightarrow \mathbb{R}^2$  are defined as its equivalence class  $[y]$  under translation, rotation, and, for shapes, scale. This is analogous to the shape/form of a landmark configuration  $\mathbf{y} \in \mathbb{R}^{k \times 2}$ , which we identify, for notational simplicity, with a function  $y : \{1, \dots, k\} \rightarrow \mathbb{R}^2$ . The shape/form representatives  $y$  are considered elements of a Hilbert space  $\mathcal{Y}$ . Although the quotient spaces of  $[y]$  present abstract Riemannian manifolds, we may pick suitable representatives  $\tilde{y} \in [y] \subset \mathcal{Y}$  and identify tangent spaces with linear subspaces of  $\mathcal{Y}$  to formulate and carry out necessary geometric operations in  $\mathcal{Y}$ . This is due to well-known results on Riemannian immersions and submersions (see, e.g., Huckemann et al., 2010; Klingenberg, 1995, for details). As for landmark shapes in Dryden and Mardia (2016), it allows us to restrict to a minimum of differential geometric language for readability without further geometric background. Starting from the Hilbert space  $\mathcal{Y}$  of representatives  $y$  of a single shape or form observation, we successively characterize its quotient space geometry under translation, rotation and re-scaling via the respective tangent spaces. Building on that, we introduce Riemannian exponential and logarithmic maps and parallel transports needed for model formulation and fitting, and introduce the sampling space of a sample of shapes/forms of (irregularly observed) curves.

To make use of complex arithmetic, we identify  $\mathbb{R}^2 \cong \mathbb{C}$ , the two-dimensional plane with the complex numbers. Accordingly, we consider a planar curve a function  $y : \mathbb{R} \supset \mathcal{T} \rightarrow \mathbb{C}$ , element of a separable complex Hilbert space  $\mathcal{Y}$  with a complex inner product  $\langle \cdot, \cdot \rangle$  and  $\|\cdot\|$  the corresponding norm. The two real-valued component functions of  $y$  are identified with the real part  $\mathcal{Re}(y)(t) = \mathcal{Re}(y(t))$  and imaginary part  $\mathcal{Im}(y)(t) = \mathcal{Im}(y(t))$  of  $y = \mathcal{Re}(y) + \mathcal{Im}(y)i$ . While the complex setup is used for convenience, the real part of  $\langle \cdot, \cdot \rangle$  constitutes the real inner product  $\mathcal{Re}(\langle y_1, y_2 \rangle) = \langle \mathcal{Re}(y_1), \mathcal{Re}(y_2) \rangle + \langle \mathcal{Im}(y_1), \mathcal{Im}(y_2) \rangle$  for  $y_1, y_2 \in \mathcal{Y}$  on the underlying space of real-valued planar curves. Typically  $\mathcal{Re}(y), \mathcal{Im}(y)$  are assumed square-integrable with respect to a measure  $\nu$  and we consider the canonical inner product  $\langle y, y' \rangle = \int y^\dagger y' d\nu$  where  $y^\dagger$  denotes the conjugate transpose of  $y$ . For a scalar  $y(t) \in \mathbb{C}$ ,  $y^\dagger(t) = \mathcal{Re}(y)(t) - \mathcal{Im}(y)(t)i$  is simply the complex conjugate, but for vectors  $\mathbf{y} \in \mathbb{C}^k$ , the vector  $\mathbf{y}^\dagger$  is also transposed. For curves, we typically assume the domain  $\mathcal{T} = [0, 1]$  with  $\nu$  the Lebesgue measure. For  $y$  representing discrete landmark point configurations, a standard choice would be  $\mathcal{T} = \{1, \dots, k\}$ , the point indices, and  $\nu$  the counting measure.

Given this functional data setup, consider a setting with the following invariances of the response curve with respect to transformations  $\mathcal{Y} \rightarrow \mathcal{Y}$  given by the group actions of translation  $\text{Trl} = \{y \xrightarrow{\text{Trl}} y + \gamma : \gamma \in \mathbb{C}\}$ , re-scaling  $\text{Scl} = \{y \xrightarrow{\text{Scl}} \lambda \cdot (y - 0_y) + 0_y : \lambda \in \mathbb{R}^+\}$  around a

reference point  $0_y \in \mathbb{C}$ , and rotation  $\text{Rot} = \{y \xrightarrow{\text{Rot}_u} u \cdot (y - 0_y) + 0_y : u \in \mathbb{S}^1\}$  around  $0_y$  with  $\mathbb{S}^1 = \{u \in \mathbb{C} : |u| = 1\} = \{\exp(i\omega) : \omega \in \mathbb{R}\}$  the circle group reflecting counterclockwise rotations by  $\omega$  radian measure. In the literature, the reference point is usually omitted setting  $0_y = 0$ , which can be done without loss of generality under translation invariance (i.e. in particular for shapes/forms). However, keeping other possible combinations of invariances in mind, we set  $0_y$  to the centroid of  $y$  in the following, given by  $0_y = \langle y, \mathbf{1} \rangle$  with  $\mathbf{1} : t \mapsto \frac{1}{\|t\|}$  the real constant function of unit norm. As long as  $\text{Trl}_\gamma(0_y) = 0_{\text{Trl}_\gamma(y)}$  as for our choice of  $0_y$ , the definition of re-scaling and rotation around  $0_y$  ensures that  $\text{Trl}_\gamma$ ,  $\text{Scl}_\lambda$  and  $\text{Rot}_u$  commute. Thus, the concatenated group actions can be written as the direct sum  $\text{Trl} + \text{Scl} + \text{Rot} = \{\text{Trl}_\gamma \circ \text{Scl}_\lambda \circ \text{Rot}_\omega : \gamma \in \mathbb{C}, \lambda \in \mathbb{R}^+, \omega \in \mathbb{S}^1\} \cong \mathbb{C} \times \mathbb{R}^+ \times \mathbb{S}^1$  and invariances with respect to  $\text{Trl}$ ,  $\text{Scl}$ ,  $\text{Rot}$  can be modularly accounted for, as required by the data problem at hand.  $\text{Trl} + \text{Rot}$ , for instance, describe rigid motions. The ultimate response object is then given by the *orbit*  $[y]_G = \{g(y) : g \in G\}$  (or short  $[y]$ ), i.e. the equivalence class with respect to the combined group action  $G$  generated by the chosen combination of  $\text{Trl}$ ,  $\text{Scl}$  and  $\text{Rot}$ .  $[y]_{\text{Trl} + \text{Scl} + \text{Rot}}$  is referred to as the *shape* of  $y$  and  $[y]_{\text{Trl} + \text{Rot}}$  as its *form* or *size-and-shape* (compare Dryden and Mardia, 2016); studying  $[y]_{\text{Scl}}$  is closely related to *directional* data analysis (Mardia and Jupp, 2009) where the direction of  $y$  is analyzed independent of its size  $\|y\|$ .

Let  $\mathcal{Y}_G = \{[y]_G : y \in \mathcal{Y}\}$  denote the quotient space of  $\mathcal{Y}$  with respect to the group action  $G$ . The description of the Riemannian geometry of  $\mathcal{Y}_G$  involves, in particular, a description of the tangent spaces  $T_{[y]}\mathcal{Y}_G$  at points  $[y] \in \mathcal{Y}_G$ , which can be considered local vector space approximations to  $\mathcal{Y}_G$  in a neighborhood of  $[y]$ . For a point  $q$  in a manifold  $\mathcal{M}$  the tangent vectors  $\beta \in T_q\mathcal{M}$  can, i.a., be thought of as gradients  $\dot{c}(0)$ , of paths  $c : \mathbb{R} \supset (-\delta, \delta) \rightarrow \mathcal{M}$  at 0 where they pass through  $c(0) = q$ . Besides their geometric meaning, they will also play an important role in the regression model, as additive model effects are formulated on tangent space level. Mapping orbits  $[y]_G$  under the different shape invariances back to suitable representatives  $\tilde{y}^G \in [y]_G \subset \mathcal{Y}$  (or short  $\tilde{y}$ ), we motivate tangent spaces as suitable linear subspaces  $T_{[y]_G}\mathcal{Y}_G \subset \mathcal{Y}$ .

**Translation invariance:** Starting with translation invariance as the simplest case, an orbit  $[y]_{\text{Trl}}$  can be one-to-one identified with its centered representative  $\tilde{y}^{\text{Trl}} = y - \langle y, \mathbf{1} \rangle \mathbf{1}$  yielding an identification  $\mathcal{Y}_{\text{Trl}} \cong \{y' \in \mathcal{Y} : \langle y', \mathbf{1} \rangle = 0\}$  with a linear subspace of  $\mathcal{Y}$ . Hence, also  $T_{[y]}\mathcal{Y}_{\text{Trl}} = \{y' \in \mathcal{Y} : \langle y', \mathbf{1} \rangle = 0\}$ . For any two  $y_1, y_2 \in \mathcal{Y}$ , the distance  $d([y_1]_{\text{Trl}}, [y_2]_{\text{Trl}}) = \|\tilde{y}_1^{\text{Trl}} - \tilde{y}_2^{\text{Trl}}\| = \min_{y'_1 \in [y_1]_{\text{Trl}}, y'_2 \in [y_2]_{\text{Trl}}} \|y'_1 - y'_2\|$  corresponds to the minimum distance of points in the orbits  $[y_1]$  and  $[y_2]$ .

**Rotation invariance:** Forms  $[y]_{\text{Trl} + \text{Rot}}$  can be treated analogously. However, for rotation orbits  $[y]_{\text{Rot}}$  there is no global identification with a Hilbert subspace, but we can find local identifications around reference points  $[p]_{\text{Rot}}$  we refer to as 'poles'. Moreover, we restrict to  $y, p \in \mathcal{Y}^* = \mathcal{Y} \setminus [0]_{\text{Trl}}$  eliminating constant functions as degenerate special cases in the translation orbit of zero. For each  $[y]_{\text{Rot}}$  in an open neighborhood around  $[p]_{\text{Rot}}$  with  $\langle \tilde{y}^{\text{Trl}}, \tilde{p}^{\text{Trl}} \rangle \neq 0$ ,  $y$  can be uniquely rotation aligned to  $p$ , yielding a one-to-one identification of  $[y]_{\text{Rot}}$  with the aligned representative given by  $\tilde{y}^{\text{Rot}} = \frac{\langle \tilde{y}^{\text{Trl}}, \tilde{p}^{\text{Trl}} \rangle}{\|\tilde{y}^{\text{Trl}}\| \|\tilde{p}^{\text{Trl}}\|} \tilde{y}^{\text{Trl}} + 0_y = \underset{y' \in [y]_{\text{Rot}}}{\text{argmin}} \|y' - p\|$  (compare Fig. 1). While  $\tilde{y}^{\text{Rot}}$  depends on  $p$ , we omit this in the notation for simplicity. The local identification of the

form  $[y]_{\text{Trl} + \text{Rot}}$  is given by  $\tilde{y}^{\text{Trl} + \text{Rot}} = \widetilde{(\tilde{y}^{\text{Trl}})^{\text{Rot}}}$  concatenating the identification for translation and rotation. We motivate tangent vectors to  $\mathcal{Y}_{\text{Trl} + \text{Rot}}^*$  via *geodesics* generalizing straight lines to curved manifolds and describing shortest paths. Due to the local identification with a subspace of  $\mathcal{Y}$ , geodesics with origin in the pole  $[p]_{\text{Trl} + \text{Rot}}$  take the form  $c(\tau) = [\tilde{p}^{\text{Trl}} + \beta\tau]_{\text{Trl} + \text{Rot}}$  with  $\beta = \lambda(\tilde{y}^{\text{Trl} + \text{Rot}} - \tilde{p}^{\text{Trl}})$  determined by some  $y \in \mathcal{Y}$  in the neighborhood of  $p$  and  $\lambda \in \mathbb{R}$ .

Since the tangent vectors at  $[p]_{\text{Trl} + \text{Rot}}$  correspond to the  $\beta = \dot{c}(0)$ , they form the tangent space  $T_{[p]} \mathcal{Y}_{\text{Trl} + \text{Rot}}^* = \{y \in \mathcal{Y} : \langle y, \hat{r} \rangle = 0, \mathcal{I}m(\langle y, p \rangle) = 0\}$  corresponding to the plane extending the half-plane of all  $y$  aligned to  $p$  (Figure 1). Note that, despite the use of complex arithmetic,  $T_{[p]} \mathcal{Y}_{\text{Trl} + \text{Rot}}^*$  is a real vector space not closed under complex scalar multiplication. In general, we consider all quotient spaces manifolds over  $\mathbb{R}$  rather than over  $\mathbb{C}$ . The corresponding geodesic distance between  $[y]_{\text{Trl} + \text{Rot}}$  and the pole  $[p]_{\text{Trl} + \text{Rot}}$  is given by  $d([y]_{\text{Rot}}, [p]_{\text{Rot}}) = \|\tilde{y}^{\text{Trl} + \text{Rot}} - \tilde{p}^{\text{Trl}}\|$  reflecting the length of the geodesic between the forms  $[y]_{\text{Trl} + \text{Rot}}$  and  $[p]_{\text{Trl} + \text{Rot}}$  and the minimum distance between the orbits as sets.

**Scale invariance:** The approach to account for scale invariance in shapes  $[y]_{\text{Trl} + \text{Rot} + \text{Scl}}$  is somewhat different to that for rotation invariance since  $\text{Scl}_\lambda$  is not isometric. Instead, orbits  $[y]_{\text{Scl}}$  are identified with their normalized representatives  $\tilde{y}^{\text{Scl}} = \frac{\tilde{y}^{\text{Trl}}}{\|\tilde{y}^{\text{Trl}}\|} + 0_y$ . This yields the concatenated local identification  $\tilde{y}^{\text{Trl} + \text{Rot} + \text{Scl}} = \widetilde{(\tilde{y}^{\text{Trl} + \text{Rot}})^{\text{Scl}}}$  for shapes. Motivated by the normalization, we borrow the well-known geometry of the sphere  $\mathbb{S} = \{y \in \mathcal{Y} : \|y\| = 1\}$ , where  $T_p \mathbb{S} = \{y \in \mathcal{Y} : \mathcal{R}e(\langle y, p \rangle) = 0\}$  is the tangent space at a point  $p \in \mathbb{S}$  and geodesics are great circles. Together with translation and rotation invariance, the shape tangent space is then given by  $T_{[p]} \mathcal{Y}_{\text{Trl} + \text{Rot} + \text{Scl}}^* = T_{[p]} \mathcal{Y}_{\text{Trl} + \text{Rot}}^* \cap T_p \mathbb{S} = \{y \in \mathcal{Y} : \langle y, \hat{r} \rangle = 0, \langle y, p \rangle = 0\}$ . The geodesic distance  $d([p]_{\text{Trl} + \text{Rot} + \text{Scl}}, [y]_{\text{Trl} + \text{Rot} + \text{Scl}}) = \arccos |\langle \tilde{y}^{\text{Trl} + \text{Rot} + \text{Scl}}, \tilde{p}^{\text{Trl} + \text{Rot} + \text{Scl}} \rangle|$  corresponds to the arc-length between the representatives. This distance is often referred to as ‘Procrustes distance’ in statistical shape analysis.

We may now define the maps needed for the regression model formulation. Hereby, both  $\tilde{y}$  and  $\tilde{p}'$  are representatives of shapes/forms  $[y], [p']$  with respect to the shape/form pole  $[p]$  (i.e. rotation aligned to  $p$ ). Generalizing straight lines to a Riemannian manifold  $\mathcal{M}$ , geodesics  $c : (-\delta, \delta) \rightarrow \mathcal{M}$  can be characterized by their ‘intercept’  $c(0) \in \mathcal{M}$  and ‘slope’  $\dot{c}(0) \in T_{c(0)} \mathcal{M}$ . The *exponential map*  $\text{Exp}_q : T_q \mathcal{M} \rightarrow \mathcal{M}$  at a point  $q \in \mathcal{M}$  is defined to map  $\beta \mapsto c(1)$  for  $c$  the geodesic with  $q = c(0)$  and  $\beta = \dot{c}(0)$ . It maps a tangent vector  $\beta$  to a point  $\text{Exp}_q(\beta) \in \mathcal{M}$  located  $d(q, \text{Exp}_q(\beta)) = \|\beta\|$  apart of the pole  $q$  in the direction of  $\beta$ . On the form space  $\mathcal{Y}_{\text{Trl} + \text{Rot}}$ , the exponential map is simply given by  $\text{Exp}_{[p]}(\beta) = [p + \beta]$ . On the shape space  $\mathcal{Y}_{\text{Trl} + \text{Rot} + \text{Scl}}$ , identification with exponential maps on the sphere yields  $\text{Exp}_{[p]}(\beta) = \left[ \cos(\|\beta\|)p + \sin(\|\beta\|) \frac{\beta}{\|\beta\|} \right]$ . In an open neighborhood  $\mathcal{U}$ ,  $q \in \mathcal{U} \subset \mathcal{M}$ ,  $\text{Exp}_q$  is invertible yielding the  $\text{Log}_q : \mathcal{U} \rightarrow T_q \mathcal{M}$  map from the manifold to the tangent space at  $q$ . For forms, it is given by  $\text{Log}_{[p]}([y]) = \tilde{y} - \tilde{p}$  and, for shapes, by  $\text{Log}_{[p]}([y]) = d([p], [y]) \frac{\tilde{y} - \langle \tilde{p}, \tilde{y} \rangle \tilde{p}}{\|\tilde{y} - \langle \tilde{p}, \tilde{y} \rangle \tilde{p}\|}$ , with  $\tilde{y}, \tilde{p}$  the form or shape representatives, respectively. Finally,  $\text{Transp}_{q, q'} : T_q \mathcal{M} \rightarrow T_{q'} \mathcal{M}$  parallel transports tangent vectors  $\varepsilon \mapsto \varepsilon'$  isometrically along a geodesic  $c(\tau)$  connecting  $q$  and  $q' \in \mathcal{M}$  such that the slopes  $\dot{c}(q) \cong \dot{c}(q')$  are identified and all angles are preserved. It is used to identify directions in both tangent spaces. For shapes,  $\text{Transp}_{[p], [p']}(\varepsilon) = \varepsilon - \langle \varepsilon, \tilde{p}' \rangle \frac{\tilde{p} + \tilde{p}'}{1 + \langle \tilde{p}, \tilde{p}' \rangle}$  takes the form of the parallel transport on a sphere replacing the real inner product with its complex pendant. Parts in  $\varepsilon$  orthogonal to the complex  $\tilde{p} - \tilde{p}'$ -plane are left unchanged while the remainder is ‘rotated’ in the plane into  $T_{[p']} \mathcal{Y}_{\text{Trl} + \text{Rot} + \text{Scl}}$ . For forms, only the  $\mathcal{I}m(\langle \varepsilon, \tilde{p}' \rangle)$  coordinate orthogonal to the real  $\tilde{p} - \tilde{p}'$ -plane is rotated as in the shape case, while the remainder of  $\varepsilon$  is left unchanged as in a linear space. This yields  $\text{Transp}_{[p], [p']}(\varepsilon) = \varepsilon - \mathcal{I}m(\langle \varepsilon, \tilde{p}' / \|\tilde{p}'\| \rangle) \frac{\tilde{p} / \|\tilde{p}\| + \tilde{p}' / \|\tilde{p}'\|}{1 + \langle \tilde{p} / \|\tilde{p}\|, \tilde{p}' / \|\tilde{p}'\| \rangle} 1$  for form tangent vectors. While this or equivalent expressions for the parallel transport in the shape case can be found, e.g., in Dryden and Mardia (2016); Huckemann et al. (2010); Cornea et al. (2017), a corresponding derivation for the form case can be found in the supplementary material.

Based on this understanding of the response space, we may now proceed to consider a sample

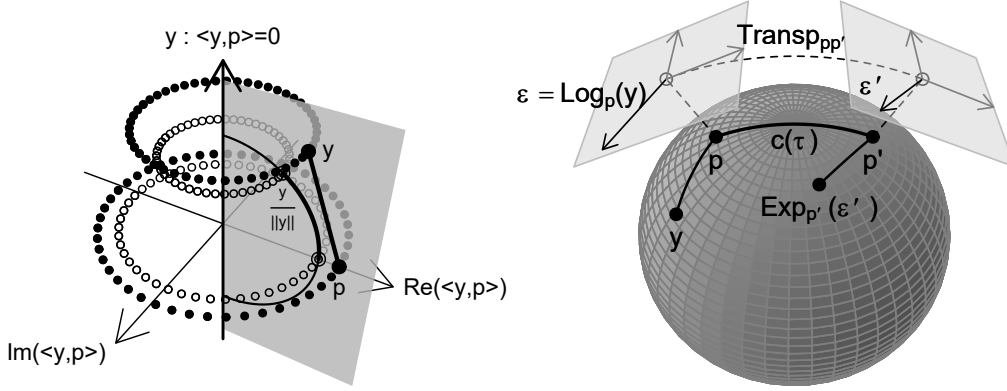


Figure 1: *Left*: Quotient space geometry: translation invariance is not depicted; given pole representative  $p$ , the orbit  $[y]_{\text{Trl} + \text{Rot}}$ , corresponding to a dotted horizontal circle in the shown coordinate system, is identified with the aligned  $y := \tilde{y}^{\text{Trl} + \text{Rot}}$  in the half-plane of  $p$ ;  $[y]_{\text{Trl} + \text{Rot} + \text{Scl}}$  is identified with the unit vector  $\tilde{y}^{\text{Trl} + \text{Rot} + \text{Scl}} = \frac{y}{\|y\|}$  projecting  $\tilde{y}^{\text{Trl} + \text{Rot}}$  onto the hemisphere depicted by the vertical semicircle. Form and shape distances between  $[p]$  and  $[y]$  correspond to those of their representatives on the plane and sphere, respectively. Thick lines describe form and shape geodesic between  $p$  and  $y$ , and  $\frac{p}{\|p\|}$  and  $\frac{y}{\|y\|}$ , respectively. *Right*: Geodesic lines, Log-map projecting  $y$  to  $\varepsilon \in T_p\mathcal{M}$ , parallel transport  $\text{Transp}_{pp'}$  forwarding  $\varepsilon$  to  $\varepsilon' \in T_{p'}\mathcal{M}$ , and Exp-map projecting  $\varepsilon'$  on  $\mathcal{M}$  illustrated for a sphere.

of curves  $y_1, \dots, y_n \in \mathcal{Y}$  representing orbits  $[y_1], \dots, [y_n]$  with respect to group actions  $G$ . In the functional case, with the domain  $\mathcal{T} = [0, 1]$ , these curves are usually observed as evaluations  $\mathbf{y}_i = (y_i(t_{i1}), \dots, y_i(t_{ik_i}))^\top$  on a finite grid  $t_{i1} < \dots < t_{ik_i} \in \mathcal{T}$  which may differ between observations. In contrast to the *regular* case with common grids, this more general data structure is referred to as *irregular* functional shape/form data. To handle this setting, we replace the original  $\langle \cdot, \cdot \rangle$  on  $\mathcal{Y}$  by an inner product  $\langle y, y' \rangle_i = \mathbf{y}_i^\top \mathbf{W}_i \mathbf{y}'_i$  on the evaluations for each observation, which provides an inner product on the  $k_i$ -dimensional space  $\mathcal{Y}_i = \mathbb{C}^{k_i}$  of the  $i$ -th response observation. The symmetric positive-definite weight matrix  $\mathbf{W}_i$  can be chosen to implement an approximation to the original measure  $\nu$  with an numerical integration measure  $\nu_i$  such as given by the trapezoidal rule. Alternatively,  $\mathbf{W}_i = \frac{1}{k_i} \mathbf{I}_{k_i}$  with the  $k_i \times k_i$  identity matrix  $\mathbf{I}_{k_i}$  presents a canonical choice. With the inner products given for  $i = 1, \dots, n$ , the sample space naturally arises as the Riemannian product  $\mathcal{Y}_{1/G}^* \times \dots \times \mathcal{Y}_{n/G}^*$  of the orbit spaces, with the individual geometries constructed as described above.

### 3 Additive Regression on Riemannian Manifolds

Consider a data scenario with  $n$  observations of a random response covariate tuple  $(Y, \mathbf{X})$ , where the realizations of  $Y$  are planar curves  $y_i : \mathcal{T} \rightarrow \mathbb{C}$ ,  $i = 1, \dots, n$ , belonging to a Hilbert space  $\mathcal{Y}$  defined as above and potentially irregularly measured on individual grids  $t_{i1} < \dots < t_{ik_i} \in \mathcal{T}$ . The response object  $[Y]$  is the equivalence class of  $Y$  with respect to translation, rotation and possibly scale and the sample  $[y_1], \dots, [y_n]$  is equipped with the respective Riemannian manifold geometry introduced in the previous section. For  $i = 1, \dots, n$ , realizations  $\mathbf{x}_i \in \mathcal{X}$  of a covariate vector  $\mathbf{X}$  in a covariate space  $\mathcal{X}$  are observed.  $\mathbf{X}$  can contain several categorical or metric covariates.

For regressing  $[Y]$  on  $\mathbf{X}$ , we propose an additive regression model analogous to functional additive regression models (cf. Greven and Scheipl, 2017) with the model equation

$$[\mu] = \text{Exp}_{[p]}(h(\mathbf{x})) = \text{Exp}_{[p]}\left(\sum_{j=1}^J h_j(\mathbf{x})\right), \quad (1)$$

where  $[\mu]$  is the conditional mean of  $[Y]$  given  $\mathbf{X} = \mathbf{x}$ . Along the lines of Cornea et al. (2017), the mean is defined via a construction that is a direct generalization of the popular linear or additive model  $Y = \mu + \varepsilon$ , where residuals  $\varepsilon$  are assumed to be independent and identically distributed with mean zero and  $\mu$  is deterministic (depending on covariates). Via the residual distribution,  $\mu$  is implicitly defined to be the mean of  $Y$ . The model does not require any particular distribution assumption (but first and typically second moments existing). In our case, the conditional mean  $[\mu]$  for any  $\mathbf{x}$ , represented by some function  $\mu \in \mathcal{Y}$ , is defined such that the local linearized residual  $\varepsilon_{[\mu]} = \text{Log}_{[\mu]}([Y])$  in  $T_{[\mu]}\mathcal{Y}_G^*$  has mean  $\mathbb{E}(\varepsilon_{[\mu]}) = \mathcal{O}$ , the zero element of  $\mathcal{Y}$ , which corresponds to  $\mathbb{E}(\varepsilon_{[\mu]}(t)) = 0$  for ( $\nu$ -almost) all  $t \in \mathcal{T}$ . Here, we assume  $[Y]$  is sufficiently close to  $[\mu]$  with probability 1 such that  $\text{Log}_{[\mu]}$  is well-defined, which is the case whenever  $\langle \tilde{Y}, \tilde{\mu} \rangle \neq 0$  for centered shape/form representatives  $\tilde{Y}$  and  $\tilde{\mu}$ , an un-restrictive and common assumption (compare also Cornea et al., 2017). However, residuals  $\varepsilon_{[\mu]}$  for different  $[\mu]$  belong to separate tangent spaces. To obtain a formulation in a common linear space instead, local residuals are mapped to residuals  $\epsilon = \text{Transp}_{[\mu],[p]}(\varepsilon_{[\mu]})$  by parallel transporting them along a geodesic from  $[\mu]$  to a common covariate independent pole  $[p]$  represented by  $p \in \mathcal{Y}$ . After this isometric mapping of all local residuals into  $T_{[p]}\mathcal{Y}_G^*$ , we can equivalently define the conditional mean  $[\mu]$  via  $\mathbb{E}(\epsilon) = \mathcal{O}$  for the transported residuals  $\epsilon$ .

$\text{Exp}_{[p]}$  maps the additive predictor  $h(\mathbf{x}) = \sum_{j=1}^J h_j(\mathbf{x}) \in T_{[p]}\mathcal{Y}_G^*$  to the response space. It is analogous to a response function in generalized linear models but depends on a pole  $[p]$ . While other response functions could be used, we restrict to the exponential map here, such that the model contains a geodesic model (Fletcher, 2013) – the direct generalization of simple linear regression – as a special case for  $h(\mathbf{x}) = \beta x_1$  with a single covariate  $x_1$  and tangent vector  $\beta$ . The pole  $[p]$  can be interpreted as an intercept. Typically, it is assumed that  $h$  is centered such that  $\mathbb{E}(h(\mathbf{X})) = \mathcal{O}$  and the pole  $[p]$  corresponds to the overall mean of  $[Y]$  defined, as the conditional mean, via residuals of mean zero. In a linear space, Model Equation (1) directly reduces to  $\mu = p + h(\mathbf{x})$ , i.e. to a standard functional additive model, where covariate effects are also usually centered to distinguish  $p$  from  $h(\mathbf{x})$ . The effect functions  $h_j$  composing the additive predictor  $h(\mathbf{x})$  are discussed in detail in the following subsection.

### 3.1 Tensor-product effect functions $h_j$

Scheipl et al. (2015) and various other authors employ tensor-product bases for specifying functional additive model terms. This approach naturally extends to tangent space bases. We model all additive terms as tensor-product effects

$$h_j(\mathbf{x}) = \sum_{r,l} \Theta_j^{(r,l)} b_j^{(l)}(\mathbf{x}) b_0^{(r)} = (\mathbf{b}_j(\mathbf{x}) \otimes \mathbf{b}_0)^\top \boldsymbol{\theta}_j$$

with a matrix of real basis coefficients  $\{\Theta_j^{(r,l)}\}_{r,l} = \boldsymbol{\Theta}_j \in \mathbb{R}^{m_0 \times m_j}$  and with the tensor-product basis elements given by the pair-wise products of  $m_0$  linear independent tangent vectors  $b_0^{(r)} \in T_{[p]}\mathcal{Y}_G^*$ ,  $r = 1, \dots, m_0$ , with  $m_j$  basis functions  $b_j^{(l)} : \mathcal{X} \rightarrow \mathbb{R}$ ,  $l = 1, \dots, m_j$ , for the  $j$ -th covariate effect depending on one or more covariates. The effect can be written in the usual vectorized



additive model notation by arranging the  $b_0^{(r)}$  and  $b_j^{(l)}$  in vectors  $\mathbf{b}_0$  and  $\mathbf{b}_j$ , combining them with a Kronecker product " $\otimes$ " to an  $m_0 \cdot m_j$  vector of tensor-product basis elements  $b_0^{(r)} \cdot b_j^{(l)}$ , and stacking the coefficients in a corresponding vector  $\boldsymbol{\theta}_j = \text{vec}(\boldsymbol{\Theta}_j) \in \mathbb{R}^{m_0 m_j}$ . While, in principle, the basis  $\mathbf{b}_0$  could also vary across effects  $j = 1, \dots, J$ , we assume a common basis for simplicity in the notation, which presents the typical choice. Occasionally, we also identify basis vectors with the sets of their elements and write, e.g.,  $\beta \in \text{span}(\mathbf{b}_0)$  for a tangent vector  $\beta$  in the span of  $\{b_0^{(1)}, \dots, b_0^{(m_0)}\}$ .

Due to the identification of  $T_{[p]}\mathcal{Y}_G^*$  with a subspace of the function space  $\mathcal{Y}$ ,  $\mathbf{b}_0$  may be specified using a common function basis used in additive models: Let  $\mathbf{b}_0^*$  be a basis of  $m_0^*$  basis functions  $\mathcal{T} \rightarrow \mathbb{C}$  in  $\mathcal{Y}$ , say a standard real-valued B-spline basis. Then we construct the tangent space basis as  $\mathbf{b}_0 = \mathbf{D}_p(\mathbf{b}_0^*, \sqrt{-1} \mathbf{b}_0^*)^\top$  with a suitable transformation matrix  $\mathbf{D}_p \in \mathbb{R}^{m_0 \times 2m_0^*}$  implementing the linear constraints given by the tangent space, i.e.  $\langle b_0^{(r)}, 1 \rangle = 0$  for translation invariance and  $\mathcal{I}m(\langle b_0^{(r)}, p \rangle) = 0$  for rotation invariance, for  $r = 1, \dots, m_0$ . The tangent space constraint  $\mathcal{R}e(\langle b_0^{(r)}, p \rangle) = 0$ , in the case of scale invariance, combines with the rotation constraint to  $\langle b_0^{(r)}, p \rangle = 0$  for shape responses.  $\mathbf{D}_p$  can be determined via QR-decomposition in practice (e.g. Wood, 2017; Stöcker et al., 2021, Online Supplement). For modeling closed curves, we additionally choose  $\mathbf{D}_p$  to enforce periodicity, i.e.  $b^{(r)}(t) = b^{(r)}(t + t_0)$  for some  $t_0 \in \mathbb{R}$  (compare Hofner et al., 2016).

Having  $\mathbf{b}_0$  specified as above, we may now use usual additive model covariate effect bases  $\mathbf{b}_j$  to modularly specify effect types from the full functional additive model 'tool box' offered by, e.g., Brockhaus et al. (2015). A 'linear effect' – linear in the tangent space – of the form  $h_j(\mathbf{x}) = \beta z$  with a scalar (typically centered) covariate  $z$  and  $\beta \in T_{[p]}\mathcal{Y}_G^*$  is simply implemented by  $\mathbf{b}_j(\mathbf{x}) = z$ . If  $z$  is the only covariate in the model, this results in a geodesic regression model: the predictions  $[\mu] = c(z) = \text{Exp}_{[p]}(\beta z)$  lie on a geodesic line  $c(z)$  moving from the 'intercept'  $c(0) = [p]$  into a constant direction determined by the 'slope'  $\dot{c}(0) = \beta$ . A smooth effect of the generic form  $h_j(\mathbf{x})(t) = f(z, t)$  can be implemented by choosing  $\mathbf{b}_j(\mathbf{x}) = (b^{(1)}(z), \dots, b^{(m_j)}(z))^\top$  a vector of, e.g., B-spline basis functions. For a categorical covariate effect of the form  $h_j(\mathbf{x}) : \{1, \dots, K\} \rightarrow T_{[p]}\mathcal{Y}_G^*$ ,  $\kappa \mapsto \beta_\kappa$ , the basis  $\mathbf{b}_j(\mathbf{x}) : \kappa \mapsto \mathbf{e}_\kappa \in \mathbb{R}^K$  maps category  $\kappa$  to a usual contrast vector  $\mathbf{e}_\kappa$  just as in standard linear models. Here, we typically use effect-encoding for obtaining centered effects. Moreover, tensor-product interactions of the model terms described above, as well as subject-specific effects and smooth effects with several additional constraints (Hofner et al., 2016) might be specified in the model formula, relying on the `mboost` framework introduced by Hothorn et al. (2010), which also allows to define custom effect designs. For identification of an overall mean intercept  $[p]$ , sum-to-zero constraints yielding  $\sum_{i=1}^n h_j(\mathbf{x}_i) = 0$  for observed covariates  $\mathbf{x}_i$ ,  $i = 1, \dots, n$ , can be specified, and similar constraints can be used to distinguish linear from non-linear effects and interactions from their marginal effects (Kneib et al., 2009). Different quadratic penalties can be specified for the coefficients  $\boldsymbol{\theta}_j$ , allowing to regularize high-dimensional effect bases and to balance effects of different complexity in the model fit. More details are given in Section 4 below.

## 3.2 Tensor-product factorization

The multidimensional and non-standard structure of the response objects makes it challenging to directly interpret and graphically illustrate additive model terms, in particular when it comes to non-linear (interaction) effects, or when effect sizes are visually small. To solve this problem, we suggest to re-write the tensor-product effect functions  $h_j$  defined for a given and fixed coefficient

vector  $\boldsymbol{\theta}_j$  as

$$h_j(\mathbf{x}) = \sum_{r=1}^{m'_j} \xi_j^{(r)} h_j^{(r)}(\mathbf{x})$$

factorized into  $m'_j = \min(m_j, m_0)$  components consisting of covariate effects  $h_j^{(r)} : \mathcal{X} \rightarrow \mathbb{R}$ ,  $r = 1, \dots, m'_j$ , in  $\text{span}(\mathbf{b}_j)$ , i.e. scalar pendants of  $h_j$ , into respective orthonormal directions  $\xi_j^{(r)} \in \text{span}(\mathbf{b}_0) \subset T_{[p]}\mathcal{Y}_G^*$  with  $\langle \xi_j^{(r)}, \xi_j^{(l)} \rangle = \mathbb{1}(r=l)$ , i.e. 1 if  $r=l$  and 0 otherwise. The components are specified to achieve decreasing predictor variances  $v_j^{(1)} \leq \dots \leq v_j^{(m'_j)}$  given by  $v_j^{(r)} = \mathbb{E}_{\mathbf{X}} \left( \langle h_j^{(r)}(\mathbf{X}), h_j^{(r)}(\mathbf{X}) \rangle \right)$ . In practice, the expectation  $\mathbb{E}_{\mathbf{X}}(\cdot)$  over the covariates  $\mathbf{X}$  is replaced by its empirical analog and the inner product  $\langle \cdot, \cdot \rangle$  by the sample inner product introduced in Section 2. Due to orthonormality, the component variances add up to the total predictor variance  $\sum_{r=1}^{m'_j} v_j^{(r)} = v_j = \mathbb{E}_{\mathbf{X}} \left( \langle h_j(\mathbf{X}), h_j(\mathbf{X}) \rangle \right)$ . Moreover, the factorization is optimally concentrated in the first components in the sense that for each  $l < m'_j$  there is no sequence of  $\xi_*^{(r)} \in \text{span}(\mathbf{b}_0)$  and  $h_*^{(r)} \in \text{span}(\mathbf{b}_j)$ ,  $r = 1, \dots, l$ , such that  $\mathbb{E}_{\mathbf{X}} \left( \|h_j(\mathbf{X}) - \sum_{r=1}^l \xi_*^{(r)} h_*^{(r)}(\mathbf{X})\|^2 \right) < \sum_{r=l+1}^{m'_j} v_j^{(r)}$ , i.e. the series of the first  $l$  components of the suggested *tensor-product factorization* yields the best rank  $l$  approximation of  $h_j$  on tangent space level. The fact that it is well-defined with the properties listed above follows directly from the Eckart-Young-Mirsky low-rank approximation theorem (e.g. Gentle, 2007) with the inner product of the tensor-product space induced by the inner products  $(b_0, b'_0) \mapsto \mathcal{R}e(\langle b_0, b'_0 \rangle)$  for  $b_0, b'_0 \in \text{span}(\mathbf{b}_0)$  and  $(b_j, b'_j) \mapsto \mathbb{E}_{\mathbf{X}}(b_j(\mathbf{X})b'_j(\mathbf{X}))$  for  $b_j, b'_j \in \text{span}(\mathbf{b}_j)$ . Re-writing  $h_j(\mathbf{x}) = \mathbf{b}_0^\top \boldsymbol{\Theta}_j \mathbf{b}_j(\mathbf{x})$ , the factorization could directly be achieved by SVD of the coefficient matrix  $\boldsymbol{\Theta}_j$ , if the bases  $\mathbf{b}_0$  and  $\mathbf{b}_j$  were already both orthonormal, and is in general achieved by SVD of a transformed version of  $\boldsymbol{\Theta}_j$ . For more details see the supplementary material.

Particularly in cases where large shares of the predictor variance are already explained by the first component(s), tensor-product factorization offers great opportunities for graphical illustration and interpretation of effects after the model fit: choosing some constant  $\tau > 0$ , the effect directions  $\xi_j^{(r)}$  can be visualized by plotting the pole representative  $p$  together with  $\text{Exp}_{[p]}(\tau \xi_j^{(r)})$  on the original level of the curves. With its direction given, the corresponding effect  $h_j^{(r)}(\mathbf{x})$  can be displayed separately in a standard scalar effect plot as for additive models after re-scaling it as  $\frac{1}{\tau} h_j^{(r)}(\mathbf{x})$ . The re-scaling with  $\tau$  does not change the effect but offers an important degree of freedom to achieve an intuitively accessible illustration of  $\xi_j^{(r)}$ . If the same  $\tau$  is chosen for all components  $r = 1, \dots, m'_j$  in all effects  $j = 1, \dots, J$ , all covariate effects share the same scale and can be compared across the plots. We suggest  $\tau = \max_j \sqrt{v_j}$ , the maximum total predictor standard deviation of an effect, as a good default choice reflecting typical variations observed in the predictor in the 'resolution' of the strongest effect.

Besides factorizing effects separately, it can also be helpful to apply tensor-product factorization to the joint additive predictor  $h(\mathbf{x})$ . This is analogously possible in the usual case where all additive effects  $h_j$  are constructed with the same tangent-space basis  $\mathbf{b}_0$ , since then  $h(\mathbf{x})$  can be written in the same form as described above for  $h_j(\mathbf{x})$ , by stacking all covariate effect bases  $\mathbf{b}_j$ . This yields a reformulation of the model equation as

$$[\mu] = \text{Exp}_{[p]} \left( \sum_{r=1}^{m'} \xi^{(r)} h^{(r)}(\mathbf{x}) \right)$$

with  $m' = \min(\sum_j m_j, m_0)$  and  $\xi^{(r)} \in \text{span}(\mathbf{b}_0) \subset T_{[p]}\mathcal{Y}_G^*$  orthonormal as above and with

the corresponding variance concentration in the first components, but now determined with respect to entire additive predictors  $h^{(r)} = \sum_{j=1}^J h_j^{(r)} \in \bigoplus_{j=1}^J \text{span}(\mathbf{b}_j)$  spanned by all covariate basis functions depending on different covariates. In this representation, the first component yields a geodesic additive model approximation where the predictor moves along a geodesic line  $c(\tau) = \text{Exp}_{[p]}(\xi^{(1)}\tau)$  with the signed distance  $\tau \in \mathbb{R}$  from the pole  $[p]$  modeled by a scalar additive predictor  $h^{(1)}(\mathbf{x})$  composed of covariate effects analogous to the original model predictor. This geodesic approximation is optimal in  $T_{[p]}\mathcal{Y}_G^*$  which should, in practice, suffice to obtain a good idea of the main direction of the model when the variance of the first component  $v^{(1)} = \mathbb{E}_{\mathbf{X}}(\|h^{(1)}(\mathbf{X})\|^2)$  is close to the total predictor variance  $v = \mathbb{E}_{\mathbf{X}}(\|h(\mathbf{X})\|^2) = \mathbb{E}_{\mathbf{X}}(d([p], [\mu])^2)$ .

The tensor-product factorization and factorized effect plot proposed above depict the model effects in a meaningful intrinsic coordinate system. We make extensive use of it in Section 5 and, thereby, illustrate its potential in three different scenarios. Higher-order SVD for tensor-product models has been used in the control engineering literature (Baranyi et al., 2013). Yet, we do not know of any other application in statistical functional or object data literature, even though it is similarly useful also for functional additive models. Hence, besides its implementation for additive models for shapes and form manifolds in the R package `manifoldboost`, we also extended the functional regression package `FDboost` by a corresponding method.

## 4 Component-wise $L_2$ -Boosting on Riemannian Manifolds

As mentioned in Section 3, the pole  $[p]$  of the Riemannian additive model described above is typically chosen as the overall mean of  $[Y]$ . Accordingly, not only the effect functions  $h_j$  but also  $[p]$  are to be estimated from the data. Section 4.1 introduces component-wise Riemannian  $L_2$ -Boosting for a given, fixed pole. Prior to the main model fit, the same fitting procedure can be employed to estimate  $[p]$ , as described in Section 4.2.

### 4.1 Component-wise Riemannian $L_2$ -Boosting algorithm

Component-wise gradient boosting (e.g. Bühlmann and Hothorn, 2007) is an iterative model fitting strategy accumulating predictors from smaller models, so called base-learners, in a step-wise procedure to built an ensemble predictor aiming at minimizing a mean loss function w.r.t. the predictor. To this end, the base-learners are fit to the negative gradient of the loss function in each iteration and the best fitting base-learner is added to the current ensemble predictor. Accordingly, gradient boosting is understood as gradient descent in the function space of predictors (Bühlmann et al., 2007). Especially when combined with re-sampling based early stopping of the algorithm, the component-wise stage-wise strategy offers inherent variable selection and shows a regularizing effect avoiding over-fitting. The latter was found particularly beneficial in high-dimensional functional response regression settings with high auto-correlation (Stöcker et al., 2021). With regression for scalar responses  $y \in \mathbb{R}$  with loss function  $\ell(y, \mu) = \frac{1}{2}(y - \mu)^2$  as prototype, boosting with respect to Euclidean least squares is typically referred to as  $L_2$ -Boosting (Bühlmann and Yu, 2003) and simplifies to repeated re-fitting of residuals  $\varepsilon = y - \mu = -\nabla_{\mu}\ell(y, \mu)$  corresponding to the negative gradient of the loss function. Similarly, when generalizing to least squares on Riemannian manifolds with the loss  $\frac{1}{2}d^2([y], [\mu])$  given by the squared geodesic distance, the negative gradient  $-\nabla_{[\mu]}\frac{1}{2}d^2([y], [\mu]) = \text{Log}_{[\mu]}([y]) = \varepsilon_{[\mu]}$  (compare e.g. Pennec, 2006) corresponds to the local residuals  $\varepsilon_{[\mu]}$  defined in Section 3. The analogy motivates the presented generalized algorithm where local residuals are further transported to residuals  $\epsilon$  in a common linear space – which is trivial in the Euclidean case.

Consider the pole  $[p]$  known and fixed for now. Aiming to minimize the population mean loss

$$\rho(h) = \mathbb{E} \left( d^2 \left( [Y], \text{Exp}_{[p]}(h(\mathbf{X})) \right) \right)$$

we fit the data by successively reducing its empirical analogue

$$\hat{\rho}(h) = \frac{1}{n} \sum_{i=1}^n d_i^2 \left( [y_i], \text{Exp}_{[p]}(h(\mathbf{x}_i)) \right)$$

where we replace the population mean by the sample mean loss and compute the geodesic distances  $d_i$  with respect to the inner products  $\langle \cdot, \cdot \rangle_i$  defined for the respective evaluations of  $y_i$ .

In each boosting step, the current residuals  $\epsilon_1, \dots, \epsilon_n$  are first computed via transporting local residuals to the predictor tangent space at  $[p]$  as defined in the model assumptions in Section 3.

Each covariate effect  $h_j = (\mathbf{b}_j(\mathbf{x}) \otimes \mathbf{b}_0)^\top \boldsymbol{\theta}_j$  constitutes an individual base-learner, which is fit to the residuals by least-squares minimizing  $\sum_{i=1}^n \|\epsilon_i - h_j(\mathbf{x}_i)\|_i^2$  where the coefficients  $\boldsymbol{\theta}_j$  are subject to a quadratic penalty of the form  $(\boldsymbol{\theta}_j)^\top \mathbf{R}_j \boldsymbol{\theta}_j$ . The  $m_j m_0 \times m_j m_0$  penalty matrix is constructed as  $\mathbf{R}_j = \lambda_j (\mathbf{P}_j \otimes \mathbf{I}_{m_0}) + \lambda_0 (\mathbf{I}_{m_j} \otimes \mathbf{P}_0)$  with marginal penalty matrices  $\mathbf{P}_j \in \mathbb{R}^{m_j \times m_j}$  and  $\mathbf{P}_0 \in \mathbb{R}^{m_0 \times m_0}$  for  $\mathbf{b}_j$  and  $\mathbf{b}_0$ , respectively (compare, e.g., Wood, 2006). Via the penalty parameters  $\lambda_j, \lambda_0$  the effective degrees of freedom of the base-learners are controlled (Hofner et al., 2011) to achieve equally 'weak' learners despite the typically large and varying number of coefficients involved in the tensor-product effects. By choosing appropriate marginal penalty matrices  $\mathbf{P}_j$  and  $\mathbf{P}_0$ , for instance imposing a second-order difference penalty for B-splines, prior assumptions, such as smoothness, can be incorporated. The basis-changes for  $\mathbf{b}_0$  via a matrix  $\mathbf{D}_p$  described in Section 3.1 are reflected in the penalty by setting  $\mathbf{P}_0 = \mathbf{D}_p^\top \mathbf{P}_0^* \mathbf{D}_p$  for a penalty matrix  $\mathbf{P}_0^*$  specified for the un-transformed basis (and analogously for transformed  $\mathbf{b}_j$ ).

In each iteration of the proposed Algorithm 1, the best-performing base-learner is added to the current ensemble additive predictor  $h(\mathbf{x})$  after multiplying it with a step-length parameter  $\eta \in (0, 1]$ . Due to the additive model structure this corresponds to a coefficient update of the selected covariate effect. Accordingly, after repeated selection, the effective degrees of freedom of a covariate effect, in general, exceed the degrees specified for the base-learner. They are successively adjusted to the data.

To avoid over-fitting, the algorithm is typically stopped early before reaching a minimum of the empirical mean loss. The stopping iteration is determined, e.g., by using re-sampling strategies such as bootstrapping or cross-validation on the level of shapes/forms.

---

*Algorithm 1: fixed pole Riemannian  $L_2$ -boosting*

---

1. Initialization:

- Specify the geometry of the response space  $\mathcal{Y}_{/G}^*$  determining in particular Exp-, Log- and Transp-maps and select the pole  $[p]$ .
- Set up the base-learners for all  $h_j$  by choosing appropriate bases  $\mathbf{b}_j$  and  $\mathbf{b}_0$  and penalty matrices  $\mathbf{R}_j$  imposing the desired degrees of freedom.
- Choose boosting hyper-parameters  $\eta$  (defaults to 0.1) and maximal number of iterations  $m_{stop}$ .
- Initialize the base-learners as  $h_j(\mathbf{x})$  with coefficient vectors  $\boldsymbol{\theta}_j = \mathbf{0}, j = 1, \dots, J$ .

2. For  $m_{stop}$  iterations repeat:

(a) Compute residuals  $\epsilon_i, i = 1, \dots, n$  given the current predictor  $h(\mathbf{x})$ :

$$\begin{aligned} [\mu_i] &\leftarrow \text{Exp}_{[p]}(h(\mathbf{x}_i)) \\ \varepsilon_{[\mu],i} &\leftarrow \text{Log}_{[\mu_i]}([y_i]) \\ \epsilon_i &\leftarrow \text{Transp}_{[\mu_i],[p]}(\varepsilon_{[\mu],i}) \end{aligned}$$

(b) Fit base-learners for all covariate effects  $h_j$  via penalized least-squares to the residuals:

$$\hat{\boldsymbol{\theta}}_j \leftarrow \underset{\boldsymbol{\theta}}{\text{argmin}} \sum_{i=1}^n \|\epsilon_i - (\mathbf{b}_j(\mathbf{x}_i) \otimes \mathbf{b}_0)^\top \boldsymbol{\theta}\|_i^2 + \boldsymbol{\theta}^\top \mathbf{R}_j \boldsymbol{\theta}$$

(c) Select best fitting base-learner

$$\hat{j} \leftarrow \underset{j}{\text{argmin}} \sum_{i=1}^n \|\epsilon_i - (\mathbf{b}_j(\mathbf{x}_i) \otimes \mathbf{b}_0)^\top \hat{\boldsymbol{\theta}}_j\|_i^2$$

(d) Update base-learner  $h_{\hat{j}}(\mathbf{x})$  by setting

$$\boldsymbol{\theta}_{\hat{j}} \leftarrow \boldsymbol{\theta}_{\hat{j}} + \eta \cdot \hat{\boldsymbol{\theta}}_{\hat{j}}$$

and keep all other  $h_j(\mathbf{x}), j \neq \hat{j}$ .

If the response curves  $y_1, \dots, y_n$  are regularly evaluated (and in particular if they, in fact, represent land-marks), this can be used for a computationally more efficient implementation. In particular, it allows to use the functional linear array model (Brockhaus et al., 2015) in the penalized least squares fit of the base-learners, which saves memory and computation time by avoiding construction of the complete tensor-product design matrix.

The  $L_2$ -Boosting framework for Additive Regression on Riemannian manifolds is available in the add-on package `manifoldboost` ([github.com/Almond-S/manifoldboost](https://github.com/Almond-S/manifoldboost)) in the open-source statistical programming software R (R Core Team, 2018). The implementation is based on the functional regression package `FDboost` (Brockhaus and Rügamer, 2018), which is in turn based on the component-wise model-based boosting package `mboost` (Hothorn et al., 2010). Quotient geometries induced by the invariances discussed in this paper are offered ready-to-use. The package is set up towards allowing extension to other Riemannian geometries in future.

## 4.2 Determining the pole as sample mean

An intrinsic unconditional mean  $[p]$  minimizing the mean squared geodesic distance  $\mathbb{E}(d^2([Y], [p]))$  is also often referred to as *Riemannian center of mass* or more specifically as *Procrustes mean* in shape analysis (Dryden and Mardia, 2016). Aiming to minimize the same loss function, we utilize the Riemannian  $L^2$ -Boosting algorithm introduced above also for unconditional mean estimation. To this end, we model  $[p]$  as

$$[p] = \text{Exp}_{[p_0]}(h_0)$$

in an intercept-only special case of our model (1). Fixing a preliminary pole  $[p_0] \in \mathcal{Y}_{/G}^*$ , a constant effect  $h_0 \in T_{[p_0]}\mathcal{Y}_{/G}^*$  is estimated with Algorithm 1 (abandoning the common effect centering). For shapes and forms, a good candidate for  $p_0$  can be obtained as the Euclidean mean of a reasonably well aligned sample  $y_1, \dots, y_n \in \mathcal{Y}$  of representatives. Another option is to set  $p_0 = y_i$  picking some  $i = 1, \dots, n$ .

## 5 Applications and Simulation

### 5.1 Shape differences in astragali of wild and domesticated sheep

Pöllath et al. (2019) identify the shapes of sheep astragali (ankle bones) as a promising object of morphometric analysis comparing different sheep populations in order to understand anatomical effects of domestication. Based on a total of  $n = 163$  shapes recorded by Pöllath et al. (2019), we model the astragalus shape in dependence of different characteristics, including domestication status (wild/feral/domesticated), sex (female/male/not available (na)), age (juvenile/subadult/adult/na), and mobility (confined/pastured/free) of the animals as categorical covariates. The sample comprises sheep of four different breeds: asiatic wild sheep (Field Museum, Chicago; Lay, 1967; Zeder, 2006), feral Soay sheep from the islands of the St. Kilda archipelago in northwest Europe (British Natural History Museum, London; Clutton-Brock et al., 1990), and domestic Karakul sheep descending from Anatolian wild sheep as well as Marsch sheep formerly widespread, i.e., in northern Germany (Museum of Livestock Sciences, Halle (Saale); Schafberg and Wussow, 2010). Each sheep astragalus shape,  $i = 1, \dots, n$ , is represented by a configuration composed of 11 selected landmarks in a vector  $\mathbf{y}_i^{\text{lm}} \in \mathbb{C}^{11}$  and two vectors of 'semi-landmarks'  $\mathbf{y}_i^{c1} \in \mathbb{C}^{14}$  and  $\mathbf{y}_i^{c2} \in \mathbb{C}^{18}$  evaluated along two outline curve segments, marked on a 2D image of the bone (dorsal perspective). In general, we could separately specify smooth function bases  $\mathbf{b}_0^{c1}$  and  $\mathbf{b}_0^{c2}$  for the curves  $y_i^{c1}$  and  $y_i^{c2}$ , respectively. Due to their systematic recording, we assume, however, that not only landmarks but also semi-landmarks are regularly observed on a fixed grid, and refrain from using smooth function bases here for simplicity. Accordingly, shape configurations can directly be identified with their evaluation vectors  $\mathbf{y}_i = (\mathbf{y}_i^{\text{lm}\top}, \mathbf{y}_i^{c1\top}, \mathbf{y}_i^{c2\top})^\top \in \mathbb{C}^{43} = \mathcal{Y}$ . Thus, the geometry of the response space  $\mathcal{Y}_{/\text{Trl} + \text{Rot} + \text{Scl}}^*$  widely corresponds to the classic Kendall's shape space geometry, with the difference that, considering landmarks more descriptive than single semi-landmarks, we choose a weighted inner product  $\langle \mathbf{y}_i, \mathbf{y}_i' \rangle = \mathbf{y}_i^\dagger \mathbf{W} \mathbf{y}_i'$  with diagonal weight matrix  $\mathbf{W}$  with diagonal  $(\mathbf{1}_{11}^\top, \frac{3}{14} \mathbf{1}_{14}^\top, \frac{3}{18} \mathbf{1}_{18}^\top)^\top$  assigning the weight of three landmarks to each outline segment. We model the astragalus shapes  $[\mathbf{y}_i] \in \mathcal{Y}_{/\text{Trl} + \text{Rot} + \text{Scl}}^*$  as

$$[\boldsymbol{\mu}_i] = \text{Exp}_{[\mathbf{p}]} \left( \boldsymbol{\beta}_{\text{status}_i} + \boldsymbol{\beta}_{\text{breed}_i} + \boldsymbol{\beta}_{\text{age}_i} + \boldsymbol{\beta}_{\text{sex}_i} + \boldsymbol{\beta}_{\text{mobility}_i} \right)$$

with the pole  $[\mathbf{p}] \in \mathcal{Y}_{/G}^*$  specified as overall mean and the conditional mean  $[\boldsymbol{\mu}_i] \in \mathcal{Y}_{/\text{Trl} + \text{Rot} + \text{Scl}}^*$  depending on the effect coded covariate effects  $x_i \mapsto \boldsymbol{\beta}_{x_i} \in T_{[\mathbf{p}]} \mathcal{Y}_{/\text{Trl} + \text{Rot} + \text{Scl}}^*$  of the respective covariate  $x_i \in \{\text{status}_i, \text{breed}_i, \text{age}_i, \text{sex}_i, \text{mobility}_i\}$ . The underlying basis  $\mathbf{b}_0$  of  $T_{[\mathbf{p}]} \mathcal{Y}_{/\text{Trl} + \text{Rot} + \text{Scl}}^*$  used for modelling is derived from the canonical basis of  $\mathbb{C}^{43}$ , i.e. from 'dummy coding' the different dimensions. For identifiability, the breed and mobility effect are centered around the status effect, as we only have data on different breeds/mobility levels for domesticated sheep. Note that accordingly the effects of breed and mobility can only be interpreted within the domesticated sheep and we cannot assess which part of the estimated effect of status 'wild' and 'feral' is in fact due to breed and mobility. All base-learners are configured to one degree of freedom by employing ridge penalties for the coefficients of the covariate bases  $\mathbf{b}_j$  while the coefficients of the response basis  $\mathbf{b}_0$  are left un-penalized. With a step-length of  $\eta = 0.1$ , 10-fold shape-wise cross-validation suggests early stopping after  $m_{\text{stop}} = 89$  boosting iterations. Due to the regular observation grid, we can make use of the functional linear array model (Currie et al., 2006; Brockhaus et al., 2015) when fitting the model for saving computation time and space. The initial model fit then took about 8 seconds on a standard computer and additional 47 seconds for cross-validation. Given the present multi-level categorical covariates, we rely on tensor-product factorization for coefficient interpretation. We write a categorical covariate effect with  $K$  levels (and  $K - 1$  degrees

of freedom due to centering) as  $\beta_{x_i} = \sum_{\kappa=1}^{K-1} \xi^{(\kappa)} \beta_{x_i}^{(\kappa)}$  with scalar effects  $x_i \mapsto \beta_{x_i}^{(\kappa)} \in \mathbb{R}$  into orthonormal directions  $\xi^{(1)}, \dots, \xi^{(K-1)} \in T_{[p]} \mathcal{Y}^*_{\text{Trl} + \text{Rot} + \text{Scl}}$  explaining a decreasing amount of variance  $v_\kappa = \frac{1}{n} \sum_{i=1}^n (\beta_{x_i}^{(\kappa)})^2, \kappa = 1, \dots, K-1$ . Figure 2 displays the variances  $v_\kappa$  reflecting the importance of each component and the effect of the domestication status, the most important covariate. We observe that the first component of the status effect explains about 2/3 of the variance of the status effect, which corresponds to over 50% of the cumulative effect variance in the model. It is salient that the effect of 'feral' is not located between 'wild' and 'domestic' in that main direction, as might be naively expected. By contrast, the second component of the effect seems to reflect the expected order and still explains a considerable amount of variance. Similar to Pöllath et al. (2019), we find only little influence of age, sex and mobility on the astragalus shape. Yet, all covariates were selected by the boosting algorithm.

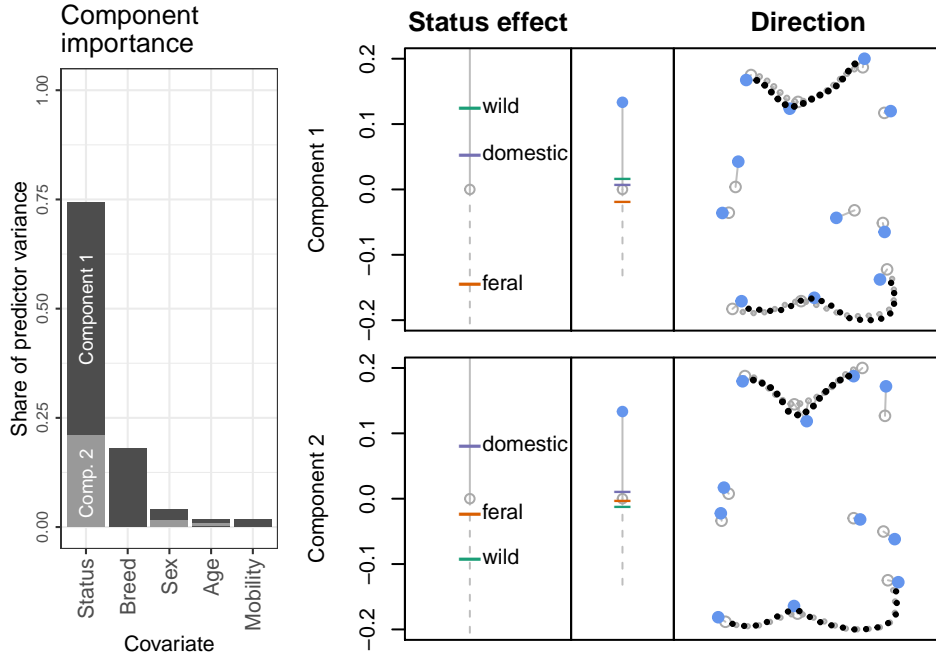


Figure 2: *Left*: Shares of different factorized covariate effects in the total predictor variance. While the variances of single orthogonal components add up to the full variance of the effect, effect variances do not exactly add up to the total predictor variance due to correlations in the covariates. *Right*: Factorized effect plots showing the two components of the status effect (*rows*): in the *right column*, the directions  $\xi^{(1)}$  and  $\xi^{(2)}$  are visualized via line-segments originating at the overall mean shape (empty circle) and ending in the shape resulting from moving 1 unit into the target direction (blue circle); in the *left column*, the status effect in the respective direction is depicted. An effect of 1 would correspond to the full extend of the direction shown on the right, which is further illustrated with a blue circle in the *middle* plot.

Visually, differences in estimated mean shapes are rather small, which is, in our experience, quite usual for shape data. With differences in size, rotation and translation excluded by definition, only comparably small variance remains in the observed shapes. Tensor-product factorization provides interpretative access: it allows to partially order the effect levels in each direction, while at the same time depicting the directions of change as accessible shape deformations.

## 5.2 Cellular Potts model parameter effects on cell form

The stochastic biophysical model proposed by Thüroff et al. (2019), a cellular Potts model (CPM), simulates migration dynamics of cells (e.g. wound healing or metastasis) in two dimensions. Modeled on a hexagonal lattice, individual cell areas evolve by successively adding or deleting single hexagons. The probability of these elementary events is determined by a Hamiltonian depending on a polarization random field inside the cell, as well as the cell expansion and other components not relevant in detail here. To match real live cell properties, different parameters controlling the Hamiltonian have to be calibrated (Schaffer, 2021). On global scale, i.e. considering whole cells, form and motion of the cells is a result of many of these local scale elementary events consecutively sampled with a Metropolis-algorithm. Thus, global scale parameter implications are not always obvious and conducting CPM simulations is comparably costly. Hence, to provide additional insights, we model the cell form in dependence of four CPM parameters considered particularly relevant. They are subsumed in a covariate vector  $\mathbf{x}_i$  for  $i = 1, \dots, n$  observations, including the real valued bulk stiffness  $x_{i1}$ , membrane stiffness  $x_{i2}$ , substrate adhesion  $x_{i3}$ , and signaling radius  $x_{i4}$ . Corresponding sampled cell outlines  $y_i$  were provided by Sophia Schaffer in context of (Schaffer, 2021), who ran underlying CPM simulations and extracted outlines of typically over 2000 cell edge hexagon locations per cell in a Cartesian coordinate system. Deriving the intrinsic orientation of the cells from their movement trajectories, we parameterized  $y_i : [0, 1] \rightarrow \mathbb{C}$ , clockwise relative to arc-length such that  $y_i(0) = y_i(1)$  points into the movement direction of the barycenter of the cell. To minimize the number of samples per curve to a more feasible mean  $\bar{k} = \frac{1}{n} \sum_{i=1}^n k_i \approx 43$  while preserving 95% of their inherent variation, we sub-sampled the curve evaluations with a greedy step-wise coarsening algorithm (described in Volkmann et al., 2021, Supplement). The resulting evaluation vectors  $\mathbf{y}_i \in \mathbb{C}^{k_i}$  were equipped with an inner-product implementing trapezoidal rule integration weights. The results shown below are based on cell samples obtained from 30 different CPM parameter configurations. For each configuration, 33 out of 10.000 Monte-Carlo cell samples were extracted as approximately independent. This yields a dataset of  $n = 990 = 30 \times 33$  cell outlines.

As positioning of the irregularly sampled cell outlines  $y_i$ ,  $i = 1, \dots, n$ , in the coordinate system is arbitrary, we model the cell forms  $[y_i] \in \mathcal{Y}_{\text{Trl} + \text{Rot}}^*$  modulo rotation and translation. Their estimated marginal form mean  $[p]$  serves as pole in the additive regression model

$$[\mu_i] = \text{Exp}_{[p]}(h(\mathbf{x}_i)) = \text{Exp}_{[p]} \left( \sum_j \beta_j x_{ij} + \sum_j f_j(x_{ij}) + \sum_{j \neq \iota} f_{j\iota}(x_{ij}, x_{i\iota}) \right)$$

where the conditional form mean  $[\mu_i]$  is modeled in dependence on different types of predictor terms. For each of the covariates  $x_{ij}$ ,  $j = 1, \dots, 4$ , the model contains a 'linear' effect with coefficient function  $\beta_j : [0, 1] \rightarrow \mathbb{C}$  and a 'non-linear' smooth effect  $f_j$  yielding a function  $f_j(x_{ij}) : [0, 1] \rightarrow \mathbb{C}$  for each value of  $x_{ij}$ . For each pair of covariates an additional smooth interaction effect  $f_{j\iota}$  is included. All involved (effect) functions are modeled via tensor-products of a tangent space basis  $\mathbf{b}_0$  of cyclic cubic P-splines, with 7 knots and a ridge penalty for  $t \in [0, 1]$  in the two curve dimensions, and quadratic P-splines, with 4 knots for the covariates  $x_{ij}$  equipped with a 2nd order difference penalty in marginal effects and ridge penalties in interactions. Covariate effects are centered to have zero mean over  $x_{ij}$ ,  $i = 1, \dots, n$ , ( $[p]$  serves as intercept) and interaction effects  $f_{j\iota}(x_j, x_\iota)$  are centered around their marginal effects  $f_j(x_j), f_\iota(x_\iota)$ , which are in turn centered around the linear effects  $\beta_j x_j$  and  $\beta_\iota x_\iota$ , respectively. Resulting predictor terms involve 69 (linear effect) to 1173 (interaction) basis coefficients but are penalized to a common degree of freedom of 2 to ensure a fair base-learner selection. We fit the model with a step-size of  $\eta = 0.25$  (instead of  $\eta = 0.1$  for faster convergence). We choose  $m_{\text{stop}} = 2000$  large enough to observe no further meaningful risk reduction, as no need for early-stopping is indicated by 10-fold form-



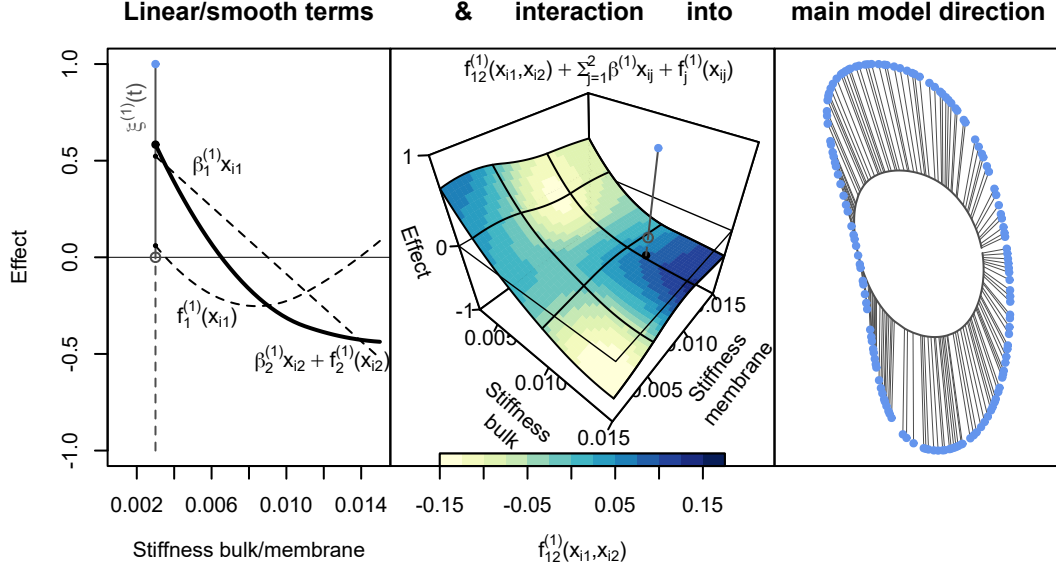


Figure 3: *Left*: Linear and non-linear effects of the stiffness bulk  $x_{i1}$ , the most important co-variate, into the main direction of the model which was determined by joint tensor-product factorization of the complete additive model predictor and explains about 93% of the total predictor variance. The effect size is depicted relative to the main direction  $\xi^{(1)}$ , which is illustrated by adding a vertical arrow of length 1 corresponding to  $\xi^{(1)}(t)$ ,  $t \in \mathcal{T}$ , in the right plot. *Right*: The overall mean cell form  $[p]$  (grey) and the form  $\text{Exp}_{[p]}(\xi^{(1)})$ , one unit into the main direction, (blue) are oriented as cells migrating to the right in the plot. *Middle*: The interaction effect of  $x_{i1}$  with the membrane stiffness  $x_{i2}$  presents the forth most important effect into the main direction (after the linear effect of the substrate adhesion  $x_{i3} \in [30, 70]$  with slope  $\beta_3^{(1)} \approx 0.009$ ). The overall effect of  $x_{i1}$  and  $x_{i2}$ , given by the sum of linear, smooth and interaction effects, is plotted as a 3D surface plot. The interaction effect  $f_{12}^{(1)}(x_{i1}, x_{i2})$  alone is added as heat map on the surface, illustrating deviations from the effect surface described by the marginal effects.

wise cross-validation. This is presumably due to the design with 33 repetitions per covariate configuration preventing over-fitting despite in-curve correlations. Due to the increased number of data points and coefficients, the irregular design, and the increased number of iterations, the model fit takes considerably longer than for the sheep astragalus model in Section 5.1, with an initial 47 minutes followed by 8 hours 46 minutes of cross-validation. However, as usual in boosting, model updates are large in the beginning and only marginal in later iterations, such that fits with  $m_{\text{stop}} = 1000$  or 500 would already give very similar results.

Observing that the most relevant components point into similar directions, we jointly factorize the additive model predictor as  $h(\mathbf{x}_i) = \sum_r \xi^{(r)} h^{(r)}(\mathbf{x}_i)$  with tensor-product factorization (Figure 3). The first component explains about 93% of the total predictor variance, indicating that, post-hoc, a good share of the model can be reduced to an additive model  $[\mu_i] = \text{Exp}_{[p]}(\xi^{(1)} h^{(1)}(\mathbf{x}_i))$  along a geodesic. Effects into the main direction  $\xi^{(1)} \in T_{[p]} \mathcal{Y}_{\text{Trl} + \text{Rot}}^*$  of the joint factorization depicted in Figure 3 show qualitatively the same picture as individual factorizations of the different effects. Among the considered CPM parameters, the bulk stiffness  $x_{i1}$  turns out to present the most important driving factor behind the cell form, explaining over 75% of the

cumulative variance of the effects. Around 80% of the effect are explained by the linear term reflecting gradual shrinkage at the side of the cells with increasing bulk value, such that simulated cells are larger and more keratocyte / croissant shaped with higher  $x_{i1}$ , and smaller and more mesenchymal shaped / elongated with lower  $x_{i1}$ . After tensor-product factorization, the non-linear part of the effect is almost entirely described by its first component which, pointing into a very similar direction as for the linear term, can be interpreted as a parabolic deviation from the linear effect. Depending also on  $x_{i1}$  and on the membrane stiffness  $x_{i2}$ , the most important interaction effect  $f_{1,2}$  explains 3.4% of the cumulative effect variance with around 98% of its variance explained by the first factorization component. All in all this means that, effectively, the entire multi-tensor-product term can be graphically illustrated and interpreted in a single factorized effect plot.

### 5.3 Realistic shape and form simulation studies

To illustrate and evaluate the proposed approach, we conduct a series of simulation studies for both form and shape regression for irregular curves. In the simulation, we compare sample sizes  $n \in \{54, 162\}$  and average grid sizes  $\bar{k} \in \{40, 100\}$  as well as an extreme case with only  $k_i = 3$  grid points for each curve but  $n = 720$ . Besides that we investigate the influence of nuisance effects and compare different inner product weights. Moreover, we check sensitivity to the orientation of curve representatives  $y_i$ ,  $i = 1, \dots, n$  in the dataset. In the following we summarize the most important results.

**Simulation design:** The true model is always of the form  $[\mu] = \text{Exp}_{[p]}(\beta_\kappa + f_1(z_1))$  with pole  $[p]$ , a binary covariate with levels  $\kappa \in \{0, 1\}$  and a smooth effect of a metric covariate  $z_1 \in [-60, 60]$ . For the response basis  $\mathbf{b}_0$  a cyclic cubic B-spline basis is chosen with 27 knots, and for the smooth effect basis  $\mathbf{b}_j$  a cubic B-spline with 4 knots. To obtain realistic and intuitively accessible scenarios, true models are obtained from fitting a dataset which was generated from the `bot` dataset from R package `Momocs` (Bonhomme et al., 2014) comprising outlines of 20 beer ( $\kappa = 0$ ) and 20 whiskey ( $\kappa = 1$ ) bottles of different brands. A metric covariate effect is induced by the 2D viewing transformations resulting from tilting the planar outlines in a 3D coordinate system along their longitudinal axis by an angle of up to 60 degree towards ( $z_1 = 60$ ) and away ( $z_1 = -60$ ) from the viewer (i.e. in a way not captured by 2D rotation invariance). Besides establishing the ground truth models based on a fit to the bottle data, we also borrow the residual structure from it: transported residuals  $\epsilon_i$  of a total of 360 outlines in the dataset are represented in the response B-spline basis. For each simulated dataset, a sample of  $\epsilon_i$  of the desired size  $n$  is randomly drawn (with replacement) and irregularly evaluated on uniformly sampled grids, with the average grid length  $\bar{k}$  varied in the simulation settings. The evaluated residuals  $\epsilon_i$  are parallel transported to  $\varepsilon_{[\mu_i],i} \in T_{[\mu_i]}\mathcal{Y}_{i/G}^*$ , the tangent space of the true conditional mean, to generate the simulated shape/form dataset  $[y_i] = \text{Exp}_{[\mu_i]}(\varepsilon_{[\mu_i],i})$ ,  $i = 1, \dots, n$ . This is done separately for shape and form response scenarios. By this approach, we preserve the typical in-curve dependence structure of realistic curve data. In for the present model fits, we choose the preliminary pole representative  $p_0$  (for estimating the pole  $[p]$ ) as a standard functional mean estimate of the curve data. Hence, the starting value of the algorithm depends on the rotation of the curves. To avoid being over-optimistic, we, thus, randomly rotate  $y_1, \dots, y_n \in \mathcal{Y}$  somewhat around the aligned form/shape representatives.

The implied residual variance on simulated datasets ranges around 105% of the predictor variance in the form scenario and around 65% in the shape scenario. All simulation settings were repeated 100 times, fitting the generated data with models including the model components specified above as well as three additional nuisance effects: a linear effect  $\beta z_1$  (orthogonal to  $f_1(z_1)$ ), an effect  $f_2$

of the same structure as  $f_1$  but depending on an independently uniformly drawn variable  $z_2$ , and a constant effect  $h_0 \in T[p]\mathcal{Y}_G^*$  to test centering around  $p$ . For the model fit, all base-learners are regularized to 4 degrees of freedom using 2nd order difference penalties for all involved B-spline basis coefficients. We specify a step-length of  $\eta = 0.1$ , and early-stopping is based on 10-fold cross-validation.

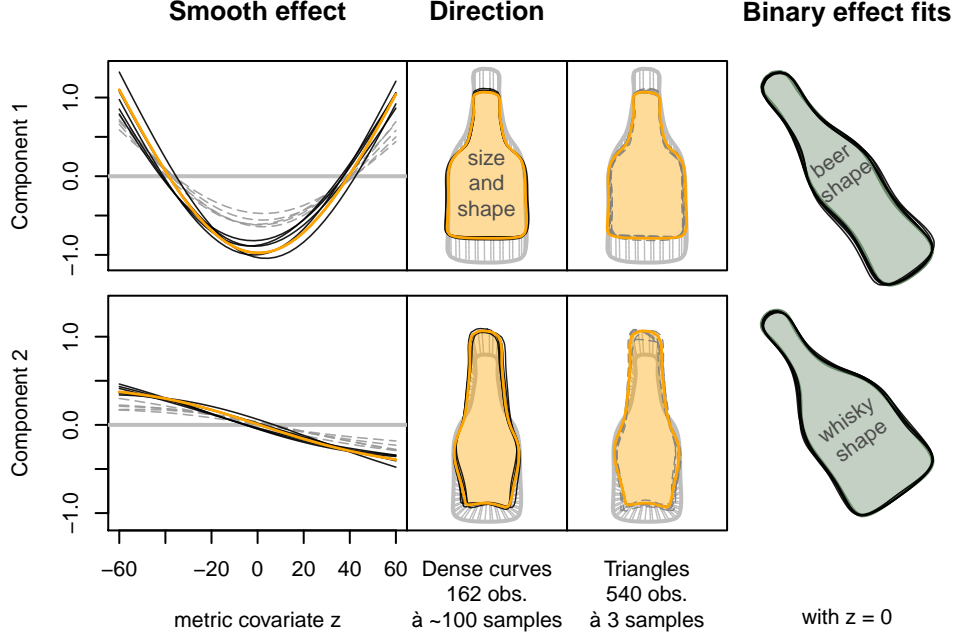


Figure 4: *Left column:* Factorized effect plot showing the first (row 1) and second (row 2) main component of smooth tensor-product effect estimates in the form scenario. Estimates of five example simulation runs (selected visually representative) are plotted for a typical setting (black solid lines) with 162 observed outlines irregularly sampled at around 100 grid points each, and an extremely sparse setting (gray dashed lines) with only 3 grid points for 720 outlines. *Middle columns:* corresponding normalized component directions are visualized as outlines resulting from following the corresponding geodesics (indicated as thin grey lines for the true underlying model) for one unit after transporting them to a common pole (grey solid outline). Accordingly, an effect of 1 corresponds to the whole extend depicted for the directions and -1 corresponds to the same extend in the opposite direction of the pole. The underlying truth is indicated by orange lines and areas, the estimates are shown as black outlines. *Right:* Five randomly selected examples of estimated shape means for both bottle types (black lines) with fixed metric covariate  $z_1 = 0$  in the shape scenario with, on average, 40 samples per outline and 54 observations. Here, olive-green areas indicate the underlying truth.

**Form scenario – smooth covariate effect:** In the form scenario, the smooth covariate effect  $f_1$  offers a particularly clear interpretation. Tensor-product factorization decomposes the true effect into its two relevant components, where the first (major) component corresponds to the bare projection of the tilted outline in 3D into the 2D image plane and the second to the additional perspective transformations (Fig. 4). For this effect, we observe a median relative

mean squared error (rMSE) of about 3.7% of the total predictor variance for small data settings with  $n = 54$  observations and a mean of  $\bar{k} = 100$  grid points (5.9% with  $\bar{k} = 40$ ), which reduces to a median rMSE of around 1.5% for a moderate size of  $n = 162$  (for both  $\bar{k} = 40$  and  $\bar{k} = 100$ ). It is typical for functional data that, from a certain point, adding more (highly correlated) evaluations per curve leads to distinctly less improvement in the model fit than adding further observations (compare, e.g., also Stöcker et al., 2021). Visual inspection of predictions, however, indicates that the denser settings indeed yield somewhat more accurate and stable predictions in high curvature domains. In the simulations, sampling is not concentrated in these regions, such that with  $\bar{k} = 40$  these ‘visual landmarks’ might still be underrepresented. To go to the extreme, we consider two scenarios with  $k_i = 3$  for all curves, i.e. where only random triangles are observed (yet, with known parameterization over  $[0, 1]$ ). With  $n = 720$  observed curves, we obtain an rMSE of around 15%, which is not surprisingly considerably higher than for the moderate settings above. Taking a closer look at the effects (Fig. 4), we find that even in this extreme setting the effect directions are captured well, while the size of the effect is underestimated. Rotation alignment based on three points (which are randomly distributed along the curves) might considerably differ from the full curve alignment, and averaging over these ‘sub-optimal’ alignments masks the full extent of the effect. Note that in the extreme  $k_i = 3$  scenario, starting with reasonably aligned  $y_i$  for estimating the overall mean  $[p]$  is necessary. For arbitrarily rotated triangles of evaluations at different grid points, there is just too few information to achieve sensible rotation alignment.

**Form scenario – binary covariate effect:** Having a simpler form, the binary effect  $\beta_\kappa$  is also estimated more accurately with an rMSE of around 1.5% of the predictor variance for  $n = 54$ ,  $\bar{k} = 100$  (1.9% for  $\bar{k} = 40$ ) and less than 0.8% for  $n = 162$  (for both  $\bar{k} = 40$  and  $\bar{k} = 100$ ). The pole estimation accuracy ranges in a similar scale. In the extreme  $k_i = 3$  case, we observe slightly over 5% rMSE for the binary effect.

**Shape scenario:** Qualitatively, the shape scenario shows a similar picture. For  $\bar{k} = 40$ , we observe median rMSEs of 2.8% of the predictor variance ( $n = 54$ ) and 2.2% ( $n = 162$ ) for  $f_1(z_1)$ , and 1.5% and 0.6% for the binary effect  $\varphi_\kappa$ . For  $\bar{k} = 100$ , accuracy is again slightly higher. The accuracy in the extreme  $k_i = 3$ ,  $n = 720$  case is also similar to forms with 14.8% median rMSE in  $f_1(z_1)$  and 7.6% for  $\beta_\kappa$ . This scenario is even more extreme for shapes, as due to the shape invariances  $k_i = 3$  is the minimum grid length possible here.

**Nuisance effects and integration weights:** The linear nuisance effect  $\beta_{z_1}$  was never selected, in neither form nor shape scenarios. As expected, omitting the nuisance effect  $f_2$ , which was part of simulations referred to above, improved median accuracy somewhat, yet only marginally. The constant nuisance effect  $h_0$  was only selected sometimes in extreme  $k_i = 3$  scenarios indicating problems the estimation of the pole  $[p]$ . Although far more effects for inherent variable selection could be included in the presented boosting approach, this is not our focus here. Thus, we refer to, e.g., Brockhaus et al. (2017) performing gradient boosting with functional responses and a large number of covariate effects with stability selection for further discussion on variable selection in a related context. Finally, simulations indicate that, inner product weights implementing a trapezoidal rule for numeric integration are slightly preferable for typical grid sizes ( $\bar{k} = 40, 100$ ), whereas weights of  $1/k_i$  equal over all grid points within a curve gave slightly better results in the extremely sparse setting with  $k_i = 3$ .

All in all, the simulations show that Riemannian  $L_2$ -Boosting can adequately fit both shape and form models in typical realistic scenarios and captures effects reasonably well even for a comparably small number of sampled outlines with a small number of observed grid points.

## 6 Discussion and Outlook

Compared to existing shape regression models (cf. Cornea et al., 2017), the presented approach extends multiple linear predictors to more general additive predictors including also e.g. smooth nonlinear model terms and interactions, and yields the first regression approach for functional shape and form responses. Moreover, we introduce a novel SVD based factorization that, similar to functional principal component analysis, enables a systematic decomposition of the variability explained by an additive effect on tangent space level. Its potential for visualization of nonlinear effects will be useful also for (univariate) functional additive models in linear spaces.

Instead of operating on the original evaluations  $\mathbf{y}_i \in \mathbb{C}^{n_i}$  of response curves  $y_i$  as in all applications above, another frequently used approach expands  $y_i$ ,  $i = 1, \dots, n$ , in a common basis first, before carrying out statistical analysis on coefficient vectors (compare e.g. Ramsay and Silverman (2005); Morris (2015) in FDA or Bonhomme et al. (2014) in shape analysis literature). This is, in fact, a special case of our approach, where the inner product is evaluated on the coefficients instead of curve evaluations, since the entire quotient space geometry and model is determined by the Hilbert space  $\mathcal{Y}$ . To illustrate this explicitly, let  $y_i \approx \mathbf{b}_0^* \top \tilde{\mathbf{y}}_i$  be expanded in the same basis  $\mathbf{b}_0^*$  used for the construction of the tensor-product effects  $h_j(\mathbf{x})$  in Section 3.1 with complex basis coefficients  $\tilde{\mathbf{y}}_i \in \mathbb{C}^{m_0^*}$ . Note that we may also represent  $h_j(\mathbf{x}) = \mathbf{b}_0^* \top \Theta_j^* \mathbf{b}_j(\mathbf{x})$  with a complex coefficient matrix  $\Theta_j^*$  instead of real coefficients. The pole  $[p] = [\mathbf{b}_0^* \top \tilde{\mathbf{p}}]$  is expanded accordingly. Then it is easy to see that modeling the mean shape/form  $[\tilde{\boldsymbol{\mu}}] = \text{Exp}_{[\tilde{\mathbf{p}}]}(\tilde{\mathbf{h}}(\mathbf{x}))$  of the coefficients  $\tilde{\mathbf{y}}_i$  as alternative ‘landmarks’ is equivalent to our presented model on the original level of curves – up to different inner products involved – if effects  $\tilde{\mathbf{h}}_j(\mathbf{x}) = \Theta_j^* \mathbf{b}_j(\mathbf{x})$  are specified on coefficient level in the tangent space at  $[\tilde{\mathbf{p}}]$ : on the original level of curves, the model induces the same tensor-product model structure  $[\boldsymbol{\mu}] = [\mathbf{b}_0^* \top \tilde{\boldsymbol{\mu}}] = \text{Exp}_{[\mathbf{b}_0^* \top \tilde{\mathbf{p}}]}(\mathbf{b}_0^* \top \tilde{\mathbf{h}}(\mathbf{x})) = \text{Exp}_{[p]}(h(\mathbf{x}))$ . Instead of  $\langle y_i, y'_i \rangle_i = \mathbf{y}_i^\top \mathbf{W}_i \mathbf{y}'_i$  for two evaluation vectors  $\mathbf{y}_i, \mathbf{y}'_i \in \mathbb{C}^{k_i}$ , we then have  $\langle y_i, y'_i \rangle_i = \tilde{\mathbf{y}}_i^\top \tilde{\mathbf{W}} \tilde{\mathbf{y}}'_i$  for curves  $y_i, y'_i \in \mathcal{Y}$  with  $\tilde{\mathbf{W}}$  the Gramian matrix of  $\mathbf{b}_0^*$ . When, for dense grids, it can be assumed that both inner products closely approximate  $\langle y_i, y'_i \rangle$  on the level of curves, the approach based on the coefficients  $\tilde{\mathbf{y}}_i$  may be computationally preferable, guaranteeing regular and typically more sparse representations demanding for operations on smaller design matrices (in particular when utilizing the linear array framework (Brockhaus et al., 2015) as proposed above).

Using the Riemannian ‘Log link function’, the proposed model is motivated by geodesic regression, presenting a direct generalization of multiple linear regression to non-linear spaces. However, here, a linear effect of a single covariate typically does not describe a geodesic when keeping other covariates fixed. Or put differently,  $\text{Exp}_{[p]}(h_1 + h_2) \neq \text{Exp}_{\text{Exp}_{[p]}(h_1)}(h_2) \neq \text{Exp}_{\text{Exp}_{[p]}(h_2)}(h_1)$  in general. In data problems with a clear effect hierarchy, it might, thus, be interesting to define a hierarchy of geodesic effects as in  $\text{Exp}_{\text{Exp}_{[p]}(h_1)}(h_2)$ . This is, for instance, relevant in mixed models for hierarchical/longitudinal study designs (Kim et al., 2017) and could be an interesting extension to our model framework. For estimation, developments in model-based boosting for generalized additive models for location, scale and shape (GAMLSS, Thomas et al., 2018) with several model predictors present a promising basis for further extensions of our model in this direction.

Often arbitrary parameterization of observed curves with potential lack of alignment or registration suggests adding re-parameterization invariance to the set of shape invariances considered in the quotient geometry of the response. Here, an ‘elastic’ extension of the proposed regression framework based on the square-root-velocity framework (Srivastava and Klassen, 2016) seems promising, which could build on our developments here but also offers new challenges. Moreover, the generality of underlying concepts encourages investigation of our approach for further

Riemannian response spaces. Besides 3D shapes, SPD matrices occurring, e.g., as covariance matrices in functional connectivity studies or diffusion tensor imaging (e.g., Zhu et al., 2009; Kim et al., 2014), or responses in a Grassmann manifold (Hong et al., 2014) might pose interesting future response objects in additive intrinsic regression, Riemannian  $L_2$ -Boosting and tensor-product factorization for effect visualization along the lines of the presented approach.

## Acknowledgement

We sincerely thank Nadja Pöllath for providing carefully recorded sheep astragalus data and important insights and comments, Sophia Schaffer for running and discussing cell simulations and providing fully processed cell outlines, and Lisa Steyer for frequent and fruitful discussions. Moreover, we gratefully acknowledge funding by grant GR 3793/3-1 from the German research foundation (DFG).

## References

- Adams, D., F. Rohlf, and D. Slice (2013). A field comes of age: geometric morphometrics in the 21st century. *Hystrix, the Italian Journal of Mammalogy* 24(1), 7–14.
- Backenroth, D., J. Goldsmith, M. D. Harran, J. C. Cortes, J. W. Krakauer, and T. Kitago (2018). Modeling motor learning using heteroscedastic functional principal components analysis. *Journal of the American Statistical Association* 113(523), 1003–1015.
- Baranyi, P., Y. Yam, and P. Várlaki (2013). *Tensor product model transformation in polytopic model-based control*. CRC press.
- Bonhomme, V., S. Picq, C. Gaucherel, and J. Claude (2014). Momocs: Outline analysis using R. *Journal of Statistical Software* 56(13), 1–24.
- Brockhaus, S., M. Melcher, F. Leisch, and S. Greven (2017). Boosting flexible functional regression models with a high number of functional historical effects. *Statistics and Computing* 27(4), 913–926.
- Brockhaus, S. and D. Rügamer (2018). *FDboost: Boosting Functional Regression Models*. R package version 0.3-2.
- Brockhaus, S., F. Scheipl, and S. Greven (2015). The Functional Linear Array Model. *Statistical Modelling* 15(3), 279–300.
- Bühlmann, P. and T. Hothorn (2007). Boosting algorithms: Regularization, prediction and model fitting (with discussion). *Statistical Science* 22(4), 477–505.
- Bühlmann, P., T. Hothorn, et al. (2007). Boosting algorithms: Regularization, prediction and model fitting. *Statistical science* 22(4), 477–505.
- Bühlmann, P. and B. Yu (2003). Boosting with the  $l_2$  loss: regression and classification. *Journal of the American Statistical Association* 98(462), 324–339.
- Cederbaum, J., M. Pouplier, P. Hoole, and S. Greven (2016). Functional linear mixed models for irregularly or sparsely sampled data. *Statistical Modelling* 16(1), 67–88.

- Chiou, J.-M., Y.-F. Yang, and Y.-T. Chen (2014). Multivariate functional principal component analysis: A normalization approach. *Statistica Sinica* 24(4), 1571–1596.
- Clutton-Brock, J., K. Dennis-Bryan, P. L. Armitage, and P. A. Jewell (1990). Osteology of the Soay sheep. *Bull. Br. Mus. Nat. Hist.* 56(1), 1–56.
- Cornea, E., H. Zhu, P. Kim, J. G. Ibrahim, and the Alzheimer’s Disease Neuroimaging Initiative (2017). Regression models on Riemannian symmetric spaces. *Journal of the Royal Statistical Society: Series B* 79(2), 463–482.
- Currie, I. D., M. Durban, and P. H. Eilers (2006). Generalized linear array models with applications to multidimensional smoothing. *Journal of the Royal Statistical Society: Series B (Statistical Methodology)* 68(2), 259–280.
- Davis, B. C., P. T. Fletcher, E. Bullitt, and S. Joshi (2010). Population shape regression from random design data. *International journal of computer vision* 90(2), 255–266.
- Dommergues, C. H., J.-L. Dommergues, and E. P. Verrecchia (2007). The discrete cosine transform, a Fourier-related method for morphometric analysis of open contours. *Mathematical Geology* 39(8), 749–763.
- Dryden, I. L. and K. V. Mardia (2016). *Statistical Shape Analysis: With Applications in R*. John Wiley & Sons.
- Fishbaugh, J., M. Prastawa, G. Gerig, and S. Durrleman (2013). *Geodesic Shape Regression in the Framework of Currents*, pp. 718–729. Berlin, Heidelberg: Springer Berlin Heidelberg.
- Fletcher, P. T. (2013). Geodesic regression and the theory of least squares on Riemannian manifolds. *International Journal of Computer Vision* 105(2), 171–185.
- Gentle, J. E. (2007). *Matrix algebra: Theory, Computations and Applications in Statistics*. Springer International Publishing.
- Goldsmith, J. and T. Kitago (2016). Assessing systematic effects of stroke on motor control using hierarchical function-on-scalar regression. *Journal of the Royal Statistical Society: Series C* 65(2), 215–236.
- Goodall, C. (1991). Procrustes methods in the statistical analysis of shape. *Journal of the Royal Statistical Society: Series B* 53(2), 285–321.
- Greven, S. and F. Scheipl (2017). A general framework for functional regression modelling (with discussion and rejoinder). *Statistical Modelling* 17(1-2), 1–35 and 100–115.
- Happ, C. and S. Greven (2018). Multivariate functional principal component analysis for data observed on different (dimensional) domains. *Journal of the American Statistical Association* 113(522), 649–659.
- Hinkle, J., P. T. Fletcher, and S. Joshi (2014). Intrinsic polynomials for regression on Riemannian manifolds. *Journal of Mathematical Imaging and Vision* 50(1), 32–52.
- Hofner, B., T. Hothorn, T. Kneib, and M. Schmid (2011). A framework for unbiased model selection based on boosting. *Journal of Computational and Graphical Statistics* 20(4), 956–971.

- Hofner, B., T. Kneib, and T. Hothorn (2016). A unified framework of constrained regression. *Statistics and Computing* 26(1-2), 1–14.
- Hong, Y., N. Singh, R. Kwitt, and M. Niethammer (2014). Time-warped geodesic regression. In *International Conference on Medical Image Computing and Computer-Assisted Intervention*, pp. 105–112. Springer.
- Hothorn, T., P. Bühlmann, T. Kneib, M. Schmid, and B. Hofner (2010). Model-based boosting 2.0. *Journal of Machine Learning Research* 11, 2109–2113.
- Huckemann, S., T. Hotz, and A. Munk (2010). Intrinsic MANOVA for Riemannian manifolds with an application to Kendall’s space of planar shapes. *IEEE Transactions on Pattern Analysis and Machine Intelligence* 32(4), 593–603.
- Kendall, D. G. (1984). Shape manifolds, Procrustean metrics, and complex projective spaces. *Bulletin of the London Mathematical Society* 16(2), 81–121.
- Kendall, D. G., D. Barden, T. K. Carne, and H. Le (1999). *Shape and shape theory*, Volume 500. John Wiley & Sons, LTD.
- Kent, J. T. (1994). The complex Bingham distribution and shape analysis. *Journal of the Royal Statistical Society: Series B* 56(2), 285–299.
- Kim, H. J., N. Adluru, M. D. Collins, M. K. Chung, B. B. Bendlin, S. C. Johnson, R. J. Davidson, and V. Singh (2014). Multivariate general linear models (mgglm) on Riemannian manifolds with applications to statistical analysis of diffusion weighted images. In *Proceedings of the IEEE Conference on Computer Vision and Pattern Recognition*, pp. 2705–2712.
- Kim, H. J., N. Adluru, H. Suri, B. C. Vemuri, S. C. Johnson, and V. Singh (2017). Riemannian nonlinear mixed effects models: Analyzing longitudinal deformations in neuroimaging. In *2017 IEEE Conference on Computer Vision and Pattern Recognition (CVPR)*, pp. 5777–5786.
- Klingenberg, W. (1995). *Riemannian geometry*. de Gruyter.
- Kneib, T., T. Hothorn, and G. Tutz (2009). Variable selection and model choice in geoaddivitive regression models. *Biometrics* 65(2), 626–634.
- Lay, D. M. (1967). A study of the mammals of iran: resulting from the street expedition of 1962-63. In *Fieldiana: Zoology* 54. Field Museum of Natural History.
- Lin, Z., H.-G. Müller, and B. U. Park (2020). Additive models for symmetric positive-definite matrices, riemannian manifolds and lie groups. *arXiv preprint arXiv:2009.08789*.
- Mardia, K. and I. Dryden (1989). Shape distributions for landmark data. *Advances in Applied Probability* 21(4), 742–755.
- Mardia, K. V. and P. E. Jupp (2009). *Directional statistics*, Volume 494. John Wiley & Sons.
- Meyer, M. J., B. A. Coull, F. Versace, P. Cinciripini, and J. S. Morris (2015). Bayesian function-on-function regression for multilevel functional data. *Biometrics* 71(3), 563–574.
- Morris, J. S. (2015). Functional Regression. *Annual Review of Statistics and its Applications* 2, 321–359.
- Morris, J. S. and R. J. Carroll (2006). Wavelet-based functional mixed models. *Journal of the Royal Statistical Society, Series B* 68(2), 179–199.



- Olsen, N. L., B. Markussen, and L. L. Raket (2018). Simultaneous inference for misaligned multivariate functional data. *Journal of the Royal Statistical Society: Series C* 67(5), 1147–1176.
- Pennec, X. (2006). Intrinsic statistics on riemannian manifolds: Basic tools for geometric measurements. *Journal of Mathematical Imaging and Vision* 25(1), 127–154.
- Pöllath, N., R. Schafberg, and J. Peters (2019). Astragalar morphology: Approaching the cultural trajectories of wild and domestic sheep applying geometric morphometrics. *Journal of Archaeological Science: Reports* 23, 810–821.
- R Core Team (2018). *R: A Language and Environment for Statistical Computing*. Vienna, Austria: R Foundation for Statistical Computing.
- Ramsay, J. O. and B. W. Silverman (2005). *Functional Data Analysis*. Springer New York.
- Rohlf, F. and J. Archie (1984). A comparison of Fourier methods for the description of wing shape in mosquitoes (diptera: Culicidae). *Systematic Biology* 33, 302–317.
- Rosen, O. and W. K. Thompson (2009). A Bayesian regression model for multivariate functional data. *Computational statistics & data analysis* 53(11), 3773–3786.
- Schafberg, R. and J. Wussow (2010). Julius Kühn. Das Lebenswerk eines agrarwissenschaftlichen Visionärs. *Züchtungskunde* 82(6), 468–484.
- Schaffer, S. A. (2021). *Cytoskeletal dynamics in confined cell migration: experiment and modelling*. PhD thesis, LMU Munich. DOI: 10.5282/edoc.28480.
- Scheipl, F., A.-M. Staicu, and S. Greven (2015). Functional additive mixed models. *Journal of Computational and Graphical Statistics* 24(2), 477–501.
- Shi, X., M. Styner, J. Lieberman, J. G. Ibrahim, W. Lin, and H. Zhu (2009). Intrinsic regression models for manifold-valued data. In *International Conference on Medical Image Computing and Computer-Assisted Intervention*, pp. 192–199. Springer.
- Srivastava, A. and E. P. Klassen (2016). *Functional and Shape Data Analysis*. Springer-Verlag.
- Stöcker, A., S. Brockhaus, S. A. Schaffer, B. von Bronk, M. Opitz, and S. Greven (2021). Boosting functional response models for location, scale and shape with an application to bacterial competition. *Statistical Modelling* (to appear).
- Thomas, J., A. Mayr, B. Bischl, M. Schmid, A. Smith, and B. Hofner (2018). Gradient boosting for distributional regression: faster tuning and improved variable selection via noncyclical updates. *Statistics and Computing* 28(3), 673–687.
- Thüroff, F., A. Goychuk, M. Reiter, and E. Frey (2019, dec). Bridging the gap between single-cell migration and collective dynamics. *eLife* 8, e46842.
- Volkman, A., A. Stöcker, F. Scheipl, and S. Greven (2021). Multivariate functional additive mixed models. *arXiv preprint arXiv:2103.06606*.
- Wood, S. (2017). *Generalized Additive Models: An Introduction with R* (2 ed.). Chapman and Hall/CRC.
- Wood, S. N. (2006). Low-rank scale-invariant tensor product smooths for generalized additive mixed models. *Biometrics* 62(4), 1025–1036.

- Yao, F., H. Müller, and J. Wang (2005). Functional data analysis for sparse longitudinal data. *Journal of the American Statistical Association* 100(470), 577–590.
- Zeder, M. A. (2006). Reconciling rates of long bone fusion and tooth eruption and wear in sheep (*Ovis*) and goat (*Capra*). *Recent advances in ageing and sexing animal bones* 9, 87–118.
- Zhu, H., Y. Chen, J. G. Ibrahim, Y. Li, C. Hall, and W. Lin (2009). Intrinsic regression models for positive-definite matrices with applications to diffusion tensor imaging. *Journal of the American Statistical Association* 104(487), 1203–1212.
- Zhu, H., R. Li, and L. Kong (2012). Multivariate varying coefficient model for functional responses. *Annals of statistics* 40(5), 2634–2666.
- Zhu, H., J. S. Morris, F. Wei, and D. D. Cox (2017). Multivariate functional response regression, with application to fluorescence spectroscopy in a cervical pre-cancer study. *Computational Statistics and Data Analysis* 111, 88–101.